



# Ultrashort pulsed laser texturing of Li-ion battery current collectors: modeling mechanical stress during cycling

Marco Negozio<sup>1</sup> · Fabrizio Moroni<sup>1</sup> · Michele Abruzzo<sup>2</sup> · Luca Romoli<sup>2</sup> · Adrian H. A. Lutey<sup>1</sup>

Received: 26 September 2025 / Accepted: 8 December 2025  
© The Author(s) 2025

## Abstract

The finite element method (FEM) is employed within COMSOL Multiphysics to simulate mechanical stress during cycling of Li-ion battery electrodes with ultrashort pulsed laser-textured current collectors. Two- and three-dimensional models of electrodes with flat (untextured) current collectors are firstly compared, after which a parametric study is performed with the 2D model to determine the effects of current collector topography and active material porosity on the resulting stress distribution during lithiation of the anode and delithiation of the cathode. The first principal stress ( $\sigma_1$ ) is evaluated within the active materials due to their fragile nature, while the Von Mises stress ( $\sigma_v$ ) is evaluated within the current collectors due to their ductile nature. Normal ( $p$ ) and shear ( $\tau$ ) contact pressures are evaluated at the interface between the two layers as indicators of the likelihood of delamination. Stress concentration at and near the interface between laser-textured current collectors and electrode active materials is shown to induce significant increases in peak stresses, with all evaluated parameters exhibiting strong dependence on the aspect ratio of the current collector surface topography. Approximately one-order-of-magnitude increases in  $\sigma_1$ ,  $p$  and  $\tau$  are observed with a texture aspect ratio of 1, while  $\sigma_v$  approximately doubles. Over the same range of parameters, the theoretical increase in interface area between the current collector and active material is approximately +130%, implying that selection of laser parameters to achieve a given surface topography must be a compromise between improving adhesion and limiting stress concentration during electrochemical cycling.

## Highlights

- FEM is employed to simulate stresses in Li-ion battery electrodes with laser-textured current collectors;
- A 2D parametric study is performed to determine effects of topography and porosity on stress distribution;
- Stress concentration induces significant increases in peak stresses compared to flat current collectors;
- Surface topography must be a compromise between adhesion and stress concentration.

**Keywords** Li-ion batteries · Laser texturing · Finite element method · Mechanical stress · Adhesion

## 1 Introduction

Lithium-ion (Li-ion) batteries are seen as a key element to improving the sustainability of global energy systems, within the transport industry as a replacement for fossil

fuels and within electricity networks for integration of intermittent renewable energy sources [1]. While stationary storage systems require very high capacity and a long lifespan, the feasibility of electrical energy storage within transport systems primarily depends on energy density, safety, cost and lifespan [2]. Though electric road vehicles have seen widespread uptake, their range and cost continue to be limiting factors [3]. Large investments continue to be made into research and production of Li-ion batteries to improve their performance and reduce costs through economies of scale [2]. The development of high energy density materials is a key part of this strategy, with spinel  $\text{LiNi}_{0.5}\text{Mn}_{1.5}\text{O}_4$  (LNMO) cathodes and composite silicon-graphite anodes seen as near-term solutions to increase energy density and

✉ Marco Negozio  
marco.negozio@unipr.it

<sup>1</sup> Dipartimento di Ingegneria dei Sistemi e delle Tecnologie Industriali, Università degli studi di Parma, Parma 43124, Italy

<sup>2</sup> Dipartimento di Ingegneria Civile e Industriale, Università di Pisa, Pisa 56122, Italy

reduce dependence on critical raw materials such as cobalt [4]. These solutions, however, present issues relating to large volumetric changes during lithiation and delithiation of electrode active materials [5]. In view of improving the sustainability of the entire production cycle, attention is also being given to replacing N-methyl-2-pyrrolidone (NMP) solvents with water-based alternatives and exploring dry electrode manufacturing [6].

Capacity fade of Li-ion batteries is due to various phenomena that depend on both cell composition and cycling conditions. These include dendrite formation, solid electrolyte interphase (SEI) layer formation, current collector corrosion, cracking of the active material and detachment of the active material from the metallic current collector, amongst others [7, 8]. While dendrite and SEI layer formation are a result of electrochemical reactions taking place during cycling, cracking and detachment of the active layer are due to mechanical stresses induced by volumetric expansion of the anode and contraction of the cathode during charging [7]. Where mechanical stresses exceed the strength of the binder or interface between the active material and current collector, cracking or detachment from the current collector leads to an increase in resistance of the cell and consequent reduction in capacity. Larger volumetric changes induced by LNMO cathodes and composite silicon-graphite anodes compared to more conventional Li-ion cell compositions exacerbate these issues [5], leading to more stringent requirements in terms of binder properties and interface adhesion with the current collector.

Further to optimization of the binder itself [9], a consolidated approach to improving contact conditions between the active material and current collector is through surface pre-treatment and conductive coatings. Chemical treatments with strong acidic or basic solutions are commonly employed to increase the surface roughness and wettability of the current collector, while carbon coatings are applied to inhibit corrosion phenomena [10–13]. Chemical treatments present issues relating to chemical handling, while offering limited control over the resulting surface topography. Laser texturing has recently been investigated as a method for increasing surface roughness in a more controlled manner while overcoming some of the drawbacks associated with chemical treatments [14–17]. While shown to increase adhesion between the current collector and active material, the impact of increasing surface roughness on mechanical stresses at and near the interface between the current collector and electrode active material has not been fully investigated due to difficulty in performing localized measurements and the multiplicity of factors influencing electrode degradation.

Nanosecond pulsed laser ablation of metals leads to ejection of material above a given threshold fluence due to rapid

expansion of superheated liquid and vaporization [18, 19]. By controlling the pulse fluence and overlap, ablation crater arrays can be created to achieve relatively large increases in surface area, or interfacial area ratio (Sdr), while avoiding complete penetration of thin metallic current collectors. Nanosecond pulsed laser texturing has been shown to increase the Sdr of aluminum and copper current collectors by more than 40%, leading to measurable increases in adhesion between the active material and current collector [20]. Peel tests performed on  $\text{LiFePO}_4$  (LFP) cathodes and graphite anodes with laser-textured current collectors have shown that the quantity of active material remaining after tests increases by up to 30% compared to untextured current collectors [14]. Scratch tests performed with similar electrodes have also shown that laser texturing can more than double the critical load at which complete penetration or detachment of the active layer takes [20].

Despite these outcomes, laser texturing with femtosecond pulses has seen greater interest in terms of electrochemical testing of complete Li-ion cells due to lower thermal loading of current collectors and negligible material removal during laser processing. Ultrashort laser pulses can be exploited to create laser-induced periodic surface structures (LIPSS), or ripples, with a period of less than 1  $\mu\text{m}$  and depth of 300–500 nm [17, 21]. Such structures are formed with negligible material removal via interference between surface plasmon polaritons and the incident laser beam on a timescale shorter than the electron-phonon relaxation time of the target surface, typically in the order of 1–10 ps for metals [22]. Highly regular periodic structures can therefore be obtained on a variety of materials with femtosecond laser pulses [22, 23]. With linear polarization, LIPSS form as a series of parallel ridges and valleys perpendicular to the laser polarization orientation. Radial, circular or azimuthal polarization can instead be exploited to produce 2D structures [24, 25]. By increasing the laser fluence, complex hierarchical structures can be produced via a combination of ablation and hydrodynamic instability [26, 27]. Direct laser interference patterning (DLIP) can also be employed to achieve complex periodic surface topographies down to the microscale. In this case, a seed beam is divided into multiple beams that are then directed onto the target surface to obtain an interference pattern via coherent overlap [28]. With ultrashort laser pulses, the resulting surface topography is a result of laser ablation within regions of high laser fluence, leading to the formation of periodic structures via material removal. Ablation with ultrashort laser pulses on a timescale shorter than the electron-phonon relaxation time leads to strong electron excitation and non-equilibrium thermodynamic responses [18], which are generally characterized by efficient material removal and a minimal heat affected zone compared to longer laser pulses. At high repetition rates,

however, heat accumulation nonetheless leads to remelting effects and residual byproducts [29, 30].

Studies have shown that the discharge capacity of  $\text{LiNi}_{0.5}\text{Co}_{0.2}\text{Mn}_{0.3}\text{O}_2$  (NCM523) cathodes improves by up to 25% following ultrashort pulsed laser texturing of aluminum current collectors with hierarchical micro/nano structures [15]. Other studies have demonstrated improvements in adhesion between ultrashort pulsed laser textured aluminum current collectors and  $\text{LiNi}_{0.8}\text{Mn}_{0.1}\text{Co}_{0.1}\text{O}_2$  (NMC811) active materials but little difference in electrochemical performance [16]. A recent study compared different ultrashort pulsed laser texturing techniques performed on copper current collectors in terms of surface topography, wettability and electrochemical performance of composite silicon-graphite anodes [17]. Further to achieving increases in capacity retention of up to 5% with laser-textured current collectors, SEM analysis of pre- and post-cycled electrodes revealed marked differences in morphology at the interface between the current collector and active material, implying that plastic (permanent) deformation had taken place. Laser texturing was found to induce more regular deformation of current collectors compared to pristine films, suggesting that changes in the stress distribution induced by laser texturing at and near the interface with the active material may have played a role in determining the electrochemical performance of the cell, further to changes in adhesion between the two materials.

As it stands, however, there is currently a lack of differentiation between the effects of texturing on active layer adhesion and mechanical stresses within the electrode materials during charge and discharge cycling. While adhesion can be directly quantified via peel or scratch tests, stresses during cycling must take into consideration expansion and contraction of the active material. Deformation and mechanical stresses within Li-ion electrodes during lithiation and delithiation have seen much attention in the literature in terms of causes, effects, monitoring, experimental analysis, modeling and management [31–35]. Conditions at the interface between the current collector and active material have, however, seen little attention, with the effects of surface roughness not considered to date to the authors' knowledge.

The present work therefore seeks to clarify this aspect by modeling mechanical stresses at and near the interface between the current collector and active material of LNMO and composite silicon-graphite Li-ion electrodes during a single charge cycle with and without laser texturing. A 3D model of electrodes with flat current collectors is firstly developed, after which a parametric study is performed with a 2D model of electrodes with flat and textured current collectors over a range of different geometries achievable via ultrashort pulsed laser texturing in terms of feature period and aspect ratio. The effects of electrode active material

porosity and stiffness on the stress distribution are also explored. Plastic deformation of metallic current collectors is accounted for using the Johnson–Cook constitutive model. Modeling outcomes show that, while potentially increasing the contact area between the current collector and electrode active material, stress concentration during cycling leads to higher peak stresses within the active material as the aspect ratio of the surface topography increases. While crack propagation within the active material and plastic deformation of the current collector may lead to some level of stress relaxation in subsequent charge–discharge cycles, electrodes with higher peak stresses during the first charge cycle are likely to experience higher stresses in subsequent cycles, as the underlying driver of stress concentration in terms of surface topography will continue to be present to some degree. The implications of these outcomes go beyond laser texturing, suggesting that surface texturing of current collectors is a compromise between improving adhesion and increasing mechanical stresses within the electrode materials.

## 2 Modeling

### 2.1 General approach

The mechanical response of LNMO and composite silicon-graphite Li-ion battery electrodes to expansion and contraction during electrochemical cycling was simulated by the finite-element method (FEM) in COMSOL Multiphysics 6.3. The Solid Mechanics solver was employed to calculate displacement, strain and stress tensor fields within the active material and current collector in electrodes resulting from lithiation and delithiation during charging. Volumetric changes were accounted for by imposing fictitious isotropic thermal expansion and contraction within the anode and cathode active materials, respectively, with thermal expansion coefficients chosen such that the simulated volumetric changes matched those expected during lithiation of the former and delithiation of the latter.

Steady-state analyses were performed, with principal stress components ( $\sigma_1, \sigma_2, \sigma_3$ ) within the current collector and active material, as well as the normal ( $p$ ) and shear contact pressures ( $\tau$ ) at the interface between the two, extracted in each case. The first principal stress ( $\sigma_1$ ) was considered an indicator of the likelihood of mechanical failure within the active material, as this stress component is associated with tensile failure of brittle materials [36]. The Von Mises stress ( $\sigma_v$ ), a function of all three principal stresses, was instead considered an indicator of the likelihood of deformation or mechanical failure of the current collector, as this equivalent stress is associated with tensile and compressive failure of ductile materials [37]. Finally, the normal and

tangential contact pressures at the interface between the current collector and active material were considered indicators of electrode failure due to adhesion issues between the two materials [38]. While this approach effectively only accounted for a single charge cycle, trends were nonetheless expected to also apply to subsequent cycles as the underlying driver of stress concentration in terms of surface topography would continue to be present to some degree.

Two- and three-dimensional FEM models were firstly developed with flat (untextured) current collectors to compare the spatial distributions and peak values of calculated stresses with the two representations, allowing the accuracy of the 2D model to be assessed. Subsequently, a comprehensive parametric study was carried out with the 2D model to investigate the influence of laser-textured surface topography and active material stiffness on stresses during electrochemical cycling.

### 2.2 Materials

Electrode current collectors were modeled as 10 μm thick copper for the anode and 20 μm thick aluminum for the cathode, with the physical and mechanical properties of both materials taken as those of the pure materials. The active layers were instead represented as equivalent homogeneous materials with the bulk density, Young’s modulus and Poisson’s ratio determined from their constituent materials and porosity. A summary of the final material properties employed within the models is presented in Table 1.

To capture the influence of porosity and composition on the stiffness of the active materials, values of Young’s modulus were estimated via Voigt (upper limit) and Reuss (lower limit) mixing rules [39], where applicable, then corrected for porosity according to [40] (see Table 2). The solid component of the anode active layer was considered

as comprising 90% graphite ( $E_{\text{graphite}} = 4.1 \text{ GPa}$ ) and 10% silicon ( $E_{\text{silicon}} = 131 \text{ GPa}$ ). The solid component of the cathode active layer was considered as comprising 100% LNMO ( $E_{\text{LNMO}} = 136 \text{ GPa}$ ). The influence of binders and additives on the stiffness of electrode active materials was not considered due to their relatively low proportions. A target porosity of  $35 \pm 5\%$  was considered, with values of 30%, 35% and 40% assessed within the parametric study to determine the effects of porosity on the resulting stress distribution during cycling. The different combinations of upper/lower limit and porosity resulted in six values of Young’s modulus for the anode active material and three values for the cathode active material layer (Table 3), representing the entire range of foreseeable values for the considered cell configuration.

Expansion during lithiation of the anode active material was imposed as +28% volumetric strain (expansion), corresponding to 10% Si content. Contraction during delithiation of the cathode active material was instead imposed as -10% volumetric strain (contraction) within the active material. As noted previously, volumetric changes were accounted for by imposing fictitious isotropic thermal expansion and contraction within the electrode active materials.

To account for the experimentally observed plastic (permanent) deformation behavior of aluminum and copper current collectors during cycling [17], the Johnson–Cook constitutive law was implemented within COMSOL Multiphysics, defining the equivalent stress as a function of plastic strain, strain rate and temperature:

$$\bar{\sigma} = [A + B (\bar{\epsilon}_{pl})^n] \left[ 1 + C \ln \left( \frac{\dot{\bar{\epsilon}}_{pl}}{\dot{\bar{\epsilon}}_0} \right) \right] \left[ 1 - \left( \frac{T - T_{ref}}{T_{melt} - T_{ref}} \right)^m \right] \quad (1)$$

where  $A, B, C, n, m$  and  $T_{melt}$  are material-specific constants taken from the literature for aluminum and copper (see Table

**Table 1** Physical and mechanical properties of electrode materials considered in FEM models

| Component                 | Composition               | Thickness | Porosity | Density                | Young’s modulus | Poisson’s ratio |
|---------------------------|---------------------------|-----------|----------|------------------------|-----------------|-----------------|
| Anode current collector   | Pure Cu                   | 10 μm     | -        | 8940 kg/m <sup>3</sup> | 17.5 GPa        | 0.34            |
| Anode active material     | 90% graphite, 10% silicon | 50 μm     | 35 ± 5%  | 2270 kg/m <sup>3</sup> | See Table 3     | 0.18            |
| Cathode current collector | Pure Al                   | 20 μm     | -        | 2700 kg/m <sup>3</sup> | 69 GPa          | 0.33            |
| Cathode active material   | 100% LNMO                 | 50 μm     | 35 ± 5%  | 4450 kg/m <sup>3</sup> | See Table 3     | 0.30            |

**Table 2** Voigt and Reuss limits for Young’s modulus of composite materials based on constituents; Young’s modulus for porous materials

| Young’s modulus calculation                                      | Equation   |   |
|--|--|---|
| Voigt Limit (upper limit):                                       | $(E_0)_{upper} = E_A f_A + E_B f_B$                  | $E_{A/B}$ : Young’s modulus, constituent A/B  |
| Reuss Limit (lower limit):                                       | $(E_0)_{lower} = \frac{E_A E_B}{E_A f_B + E_B f_A}$  | $f_{A/B}$ : Volume fraction, constituent A/B; $\rho$ : porosity                               |
| Calculation of Young’s modulus: (porosity range [30%, 35%, 40%]) | $E_c = E_0 \left( 1 - \frac{\rho}{\rho_c} \right)^f$ | $\rho_c = 1$ [41]: critical porosity; $E_0$ : Young modulus of solid material; $f = 2.1$ [40] |

**Table 3** Values of young’s modulus considered in FEM models

| Silicon-graphite composite (anode), $E_{Si-C}$ |             |              |             |              |             |
|--|-------------|--------------|-------------|--------------|-------------|
| 30% porosity                                   |             | 35% porosity |             | 40% porosity |             |
| Upper limit                                    | Lower limit | Upper limit  | Lower limit | Upper limit  | Lower limit |
| 7.97 GPa                                       | 2.14 GPa    | 6.79 GPa     | 1.84 GPa    | 5.74 GPa     | 1.55 GPa    |
| LNMO (cathode), $E_{LNMO}$                     |             |              |             |              |             |
| 0% porosity                                    |             | 35% porosity |             | 40% porosity |             |
| 64.3 GPa                                       | 55.0 GPa    | 46.5 GPa     |             |              |             |

4. for relevant values),  $\bar{\epsilon}_{pl}$  is the equivalent plastic strain,  $\dot{\epsilon}_{pl}$  the strain rate (normalized with the reference parameter  $\dot{\epsilon}_0$ ) and  $T$  is the instantaneous temperature. This nonlinear model, which couples work-hardening with strain-rate sensitivity and thermal softening, was implemented to capture the progressive stress relaxation and reduced peak stresses associated with plastic flow within the current collectors. Because the operating temperatures of Li-ion batteries and material strain rates are generally too low to activate related phenomena in aluminum or copper [42], thermal softening and strain rate factors were effectively removed from the present analysis, simplifying the constitutive model to the isothermal form  $\bar{\sigma} = A + B(\bar{\epsilon}_{pl})^n$ . The inclusion of material yielding and strain hardening within the model nonetheless reduced peak stress predictions and yielded a stress–strain response that was more representative of experimental deformation than would have been obtained with an elastic-only model.

### 2.3 Surface topography of laser-textured current collectors

The range of surface topographies considered for laser-textured current collectors was based on typical outcomes obtained with ultrashort laser pulses on metallic surfaces, including sub-micrometric LIPSS and periodic surface structures produced via DLIP [17, 28]. With the aim of determining general trends relating to a range of surface topographies, only planar geometries were considered to allow a 2D model to be employed. While this effectively excluded more complex geometries such as 2D-LIPSS [25], the selected approach allowed the effects of surface period and aspect ratio to be thoroughly investigated by reducing the calculation time from approximately one day for 3D simulations to several minutes for 2D simulations on a workstation with an

**Table 4** Relevant constants employed for Johnson-Cook constitutive law in FEM models

| Material                | $A$ [MPa] | $B$ [MPa] | $n$  |
|-------------------------|-----------|-----------|------|
| Aluminum (cathode) [43] | 129       | 200       | 0.45 |
| Copper (anode) [44]     | 90        | 292       | 0.31 |

18-core Intel i9 processor and 128 GB of RAM. Sinusoidal surface structures with a period ( $\lambda$ ) of 1–10  $\mu\text{m}$  and aspect ratio ( $H/\lambda$ ) of 0.1–1.1 were chosen to broadly represent LIPSS and DLIP as follows, with typical ranges achievable with LIPSS and DLIP provided in Table 5:

$$z = \frac{H}{2} \sin\left(\frac{2\pi}{\lambda} x\right), \quad 1\mu\text{m} \leq \lambda \leq 10\mu\text{m}, \quad 0.1 \leq H/\lambda \leq 1 \quad (2)$$

LIPSS can be manufactured with a relatively simple setup by scanning a focused ultrashort pulsed laser beam over the target surface with specific values of pulse fluence and overlap. Low spatial frequency LIPSS are typically characterized by a series of parallel ridges and valleys with a period below the laser wavelength, in the range 700–1000 nm at a wavelength of 1030 nm and 150–250 nm at a wavelength of 343 nm [22, 23, 45]. Typically, the aspect ratio of low spatial frequency LIPSS is in the range 0.3–0.6 [17]. High spatial frequency LIPSS are instead characterized by a smaller period, down to one tenth of the laser wavelength [49]. At higher pulse fluence and overlap, more complex hierarchical structures such as  $\mu$ -grooves [17] and spikes [24] can be achieved.

Although requiring a more complex optical setup achieving division of a seed beam into multiple beams and subsequent coherent overlap [28], DLIP is a more versatile approach to independently tailor the period and aspect ratio of laser-textured surfaces. A planar interference pattern is obtained with two laser beams, while more complex patterns can be obtained with additional beams. The resulting spatial period of the obtained surface topography is a function of the laser wavelength and half angle between the incident beams [46], while the resulting depth is a function of the incident laser fluence and number of pulses. Ultrashort pulsed DLIP has been employed to achieve a wide variety of sinusoidal topographies on metallic surfaces with spatial periods of  $\lambda \leq 1\mu\text{m}$  [17, 28, 48],  $\lambda = 2.6\text{--}5.2\mu\text{m}$  [46, 47] and larger [50], including aspect ratios up to approximately 1 [46].

While sinusoidal surface structures broadly represent the ideal geometry of LIPSS and DLIP, more complex surface topographies are obtained in practice due to variations in laser energy dose, complex hydrodynamic effects and the presence of residual byproducts. While simplification of the surface geometry inevitably leads to deviations between

**Table 5** Typical surface topography ranges achievable with LIPSS and DLIP

| Type of laser texturing | Period ( $\lambda$ )                               | Aspect ratio ( $H/\lambda$ ) |
|-------------------------|--|------------------------------|
| LIPSS                   | < 1 $\mu\text{m}$ [22, 23, 45]                     | 0.3-0.6 [17]                 |
| DLIP                    | 1 $\mu\text{m}$ -10+ $\mu\text{m}$ [17, 28, 46-48] | 0-1 [46]                     |

the simulated and actual stress states, this approach was adopted as a compromise between accurately representing the surface topography for as wide a range of conditions as possible and ensuring that a sufficiently large simulation domain size could be employed to accurately represent the central zone of electrodes. This approach allowed the effects of the texture period and aspect ratio to be explored with the aim of determining overall trends and guiding future experiments. While surface features smaller than  $1\ \mu\text{m}$  are commonly reported in the literature, a lower limit of  $1\ \mu\text{m}$  was imposed in the present work due to practical limitations in terms of the number of finite elements that could practically be employed in numerical simulations while realistically modeling the surface topography and maintaining a sufficiently large calculation domain size to accurately represent the central zone of electrodes. Furthermore, as will be shown in Sect. 3, the texture period was found to be of relatively low influence on the resulting stress state in comparison to the aspect ratio.

## 2.4 3D model

A 3D FEM model was firstly developed for flat (untextured) current collectors coated on one side with active materials. The geometry and constraints employed within the 3D model are illustrated in Fig. 1. Electrode materials and thicknesses were as defined in Tables 1 and 3, with a bonded contact condition considered between the current collector and active material as no relative displacement was expected between the two. While frictional or rough contact conditions could potentially allow shear transfer mechanisms, sliding effects and incomplete contact to be accounted for, a bonded contact condition was considered most appropriate for modeling new electrodes in the present case to provide a consistent comparison between different electrodes. To obtain representative results, electrode areas of  $250\ \mu\text{m} \times 250\ \mu\text{m}$  were simulated, with symmetry boundary conditions imposed on the XZ and YZ planes to effectively double the lateral dimensions and

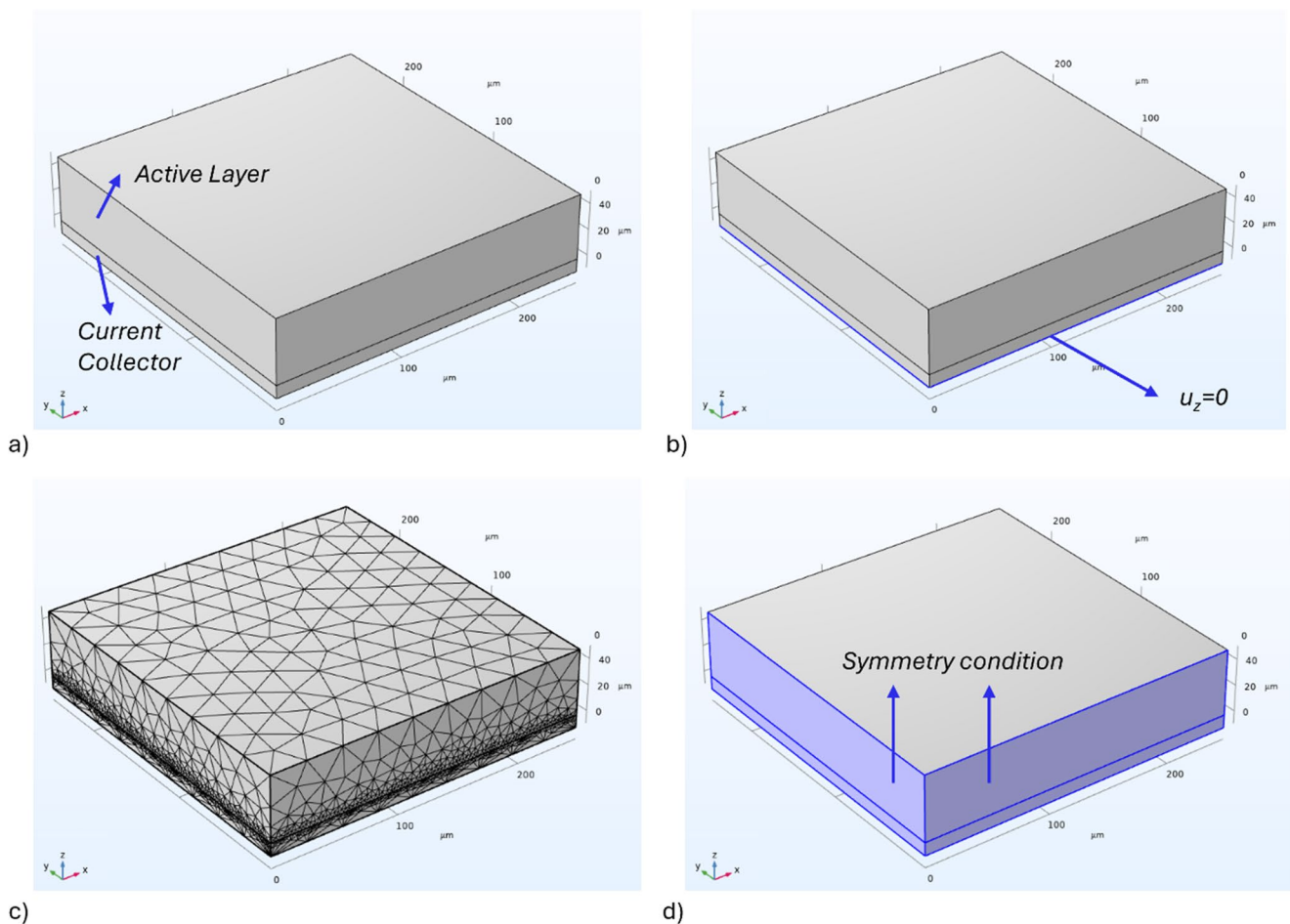


**Fig. 1** Three-dimensional FEM model: (a) electrode geometry and components, (b) fixed displacement condition applied to bottom surface, (c) mesh, (d) symmetry conditions applied to XZ and YZ planes

constrain transverse displacements to zero along the same planes. Modeled areas were therefore approximately 7–8× the thickness of each electrode (Table 1), ensuring that edge effects were correctly accounted for. Adequacy of the modeled area in representing complete cells, typically several cm<sup>2</sup>, was assessed through convergence analysis by progressively increasing the simulated area until the stress field at the center of the electrode was no longer significantly influenced by the size of the simulated area. A fixed displacement condition was applied to the bottom surface of the current collector, enforcing a null vertical displacement along this plane to inhibit rigid-body motion. Horizontal displacement was left unconstrained, allowing the electrode to deform within the plane without artificial lateral confinement. Flexural deformation was not considered, as electrodes in the majority of assembled cells are tightly stacked within a multilayer laminate, where the packing configuration effectively suppresses bending through mutual support of adjacent layers [51].

Meshing was performed with tetrahedral elements of minimum size 3 μm at the interface between the current collector and active material, maximum growth rate of 1.6 and maximum size of 30 μm at the upper surface of the active material, resulting in 123,669 elements and 22,349 nodes for the anode and 163,652 elements and 28,615 nodes for the cathode. More refined mesh was employed at and near the interface between the current collector and active material due to concentration of stresses within this region as adhesion of the active material to the current collector constrained volumetric changes of the former. Final mesh dimensions were chosen through convergence analysis by progressively reducing the size of elements until the calculated stresses were no longer significantly influenced by this parameter. An example of the resulting mesh is reported in Fig. 1.

Results of 3D FEM simulations in terms of principal stress components ( $\sigma_1$ ,  $\sigma_2$ ,  $\sigma_3$ ) and normal and shear contact stresses resulting from volumetric changes of the electrode active materials were subsequently compared with results obtained with 2D simulations in the same configuration to assess the reliability of the latter in effectively representing the stress state in complete electrodes.

## 2.5 2D model and parametric study

A 2D FEM model was initially developed to replicate the same conditions as in the 3D model in terms of electrode configurations (Tables 1 and 3) and length (250 μm). As with the 3D model, a sensitivity analysis was performed by varying the specimen length under expansion and contraction conditions, confirming that the stress in the central

region remained constant regardless of overall specimen size, thus indicating that the selected boundary conditions did not affect the results. The geometry and constraints employed within the 2D model are illustrated in Fig. 2. A symmetry boundary condition was again introduced, in this case along the plane  $x=0$ , to effectively double the length of the electrode and constrain the transverse displacement to zero along the same plane. A fixed displacement condition was once more applied to the bottom surface of the current collector, enforcing null vertical displacement to mimic mechanical support provided by the cell casing. A plane stress condition was adopted to allow in-plane expansion and contraction without constraining out-of-plane deformation. Both plane stress and plane strain formulations were evaluated during preliminary studies; however, plane stress was found to more accurately reproduce the distributions of  $\sigma_1$  and von Mises stress obtained from the corresponding 3D simulation. This modeling choice was validated by comparing results with those obtained with the 3D model in terms of the main stress components influencing the likelihood of electrode failure.

Expansion of the anode active material and contraction of the cathode active material were first simulated with flat (untextured) current collectors coated on one side, to allow direct comparison with the 3D model in terms of the resulting principal stresses ( $\sigma_1$ ,  $\sigma_2$ ,  $\sigma_3$ ) and normal and shear contact pressures. Subsequently, a comprehensive parametric study was conducted to investigate the effects of the current collector surface topography upon laser texturing and active material porosity on the resulting stresses. The interface morphology between the current collector and active material was described by Eq. (2), with simulations performed for periods ( $\lambda$ ) of 1, 2, 4, 6, 8 and 10 μm, aspect ratios ( $H/\lambda$ ) of 0.1, 0.2, 0.4, 0.6, 0.8 and 1, and values of Young's modulus as listed in Table 3, considering all combinations.

Meshing was performed with triangular elements of minimum size 0.005 μm at the interface between the current collector and active material, maximum growth rate of 1.1 and maximum size of 2.5 μm at the upper surface of the active material, resulting in 6040 elements and 3145 nodes for the anode and 7048 elements and 3653 nodes for the cathode with flat current collectors, and up to 1,224,086 elements and 612,359 nodes for the anode and 1,233,801 elements and 617,158 nodes for the cathode with laser-textured current collectors. Final mesh dimensions were again chosen through convergence analysis by progressively reducing the size of elements until the calculated stresses were no longer significantly influenced by this parameter. An example of the resulting mesh is reported in Fig. 2 for flat and laser-textured anodes.

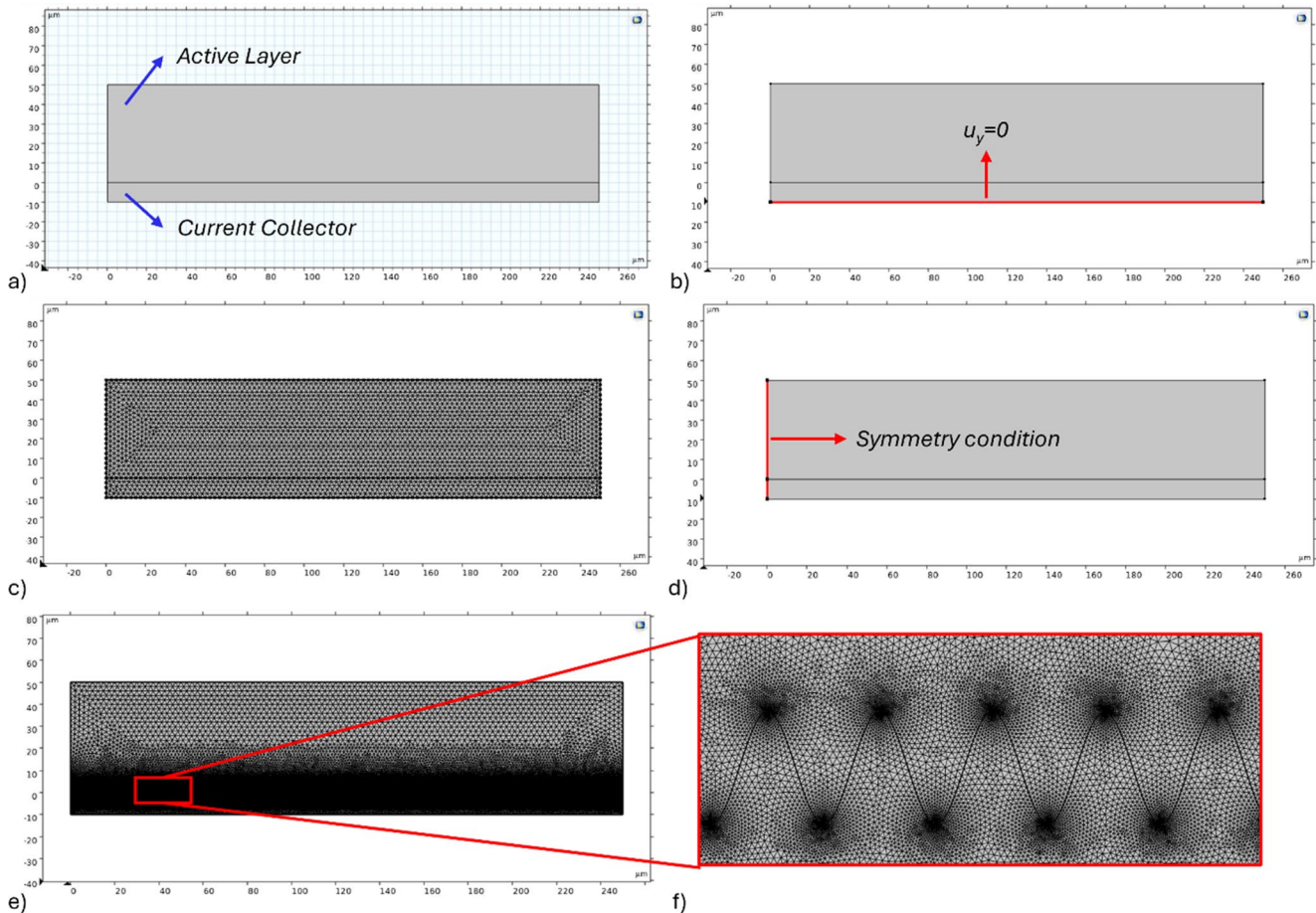


**Fig. 2** Two-dimensional FEM model: (a) electrode geometry and components, (b) fixed displacement condition applied to bottom surface, (c) mesh with flat current collector, (d) symmetry conditions applied

to  $x=0$  plane, (e) example of mesh with laser-textured current collector ( $\lambda=8 \mu\text{m}$ ,  $H/\lambda=1$ ), (f) detail of mesh with laser-textured current collector

### 3 Results and discussion

#### 3.1 3D model

Figure 3 presents the simulated spatial distributions of the three principal stresses ( $\sigma_1$ ,  $\sigma_2$ ,  $\sigma_3$ ) calculated with the 3D model for expansion of the active material ( $E=2.14 \text{ GPa}$ ) during lithiation of the anode with a flat (untextured) current collector, both as general 3D views and within the XZ cross-section. Additional insets in the same figure present the principal stresses within the active layer and current collector at the interface between the two materials. During lithiation, the first principal stress ( $\sigma_1$ ) within the active layer remains essentially zero, reflecting the isotropic nature of expansion, with no preferential tensile orientation. The stiffer current collector is instead subject to relatively high tensile stresses due to expansion of the active layer, reaching approximately +350 MPa. The second principal stress ( $\sigma_2$ ) within the active layer exhibits slight compressive stresses, reaching approximately -65 MPa, caused by biaxial restraint

in the plane orthogonal to the principal expansion direction. Within the current collector,  $\sigma_2$  mirrors  $\sigma_1$ , reaching almost +350 MPa, due to its elastic coupling to the active layer. The third principal stress ( $\sigma_3$ ) within the active layer aligns closely with  $\sigma_2$ , reaching approximately +65 MPa, while at the interface with the current collector, it decreases to nearly zero, indicating that out-of-plane constraints are minimal in this direction.

Figure 4 presents the simulated spatial distribution of the three principal stresses for contraction of the active material ( $E=55.0 \text{ GPa}$ ) during delithiation of the cathode with a flat (untextured) current collector. Within the central region of the sample ( $x=0$ ,  $y=0$ ), values of  $\sigma_1$  within the active layer tend to be slightly positive, approximately +80 MPa, gradually increasing towards the top of the layer to reach a peak of approximately +250 MPa. The current collector also exhibits a slightly tensile  $\sigma_1$  stress of approximately +30 MPa at  $x=0$ ,  $y=0$ , which decreases towards the edge to reach slightly compressive values of approximately -30 MPa before increasing again due to edge effects. Values of  $\sigma_2$

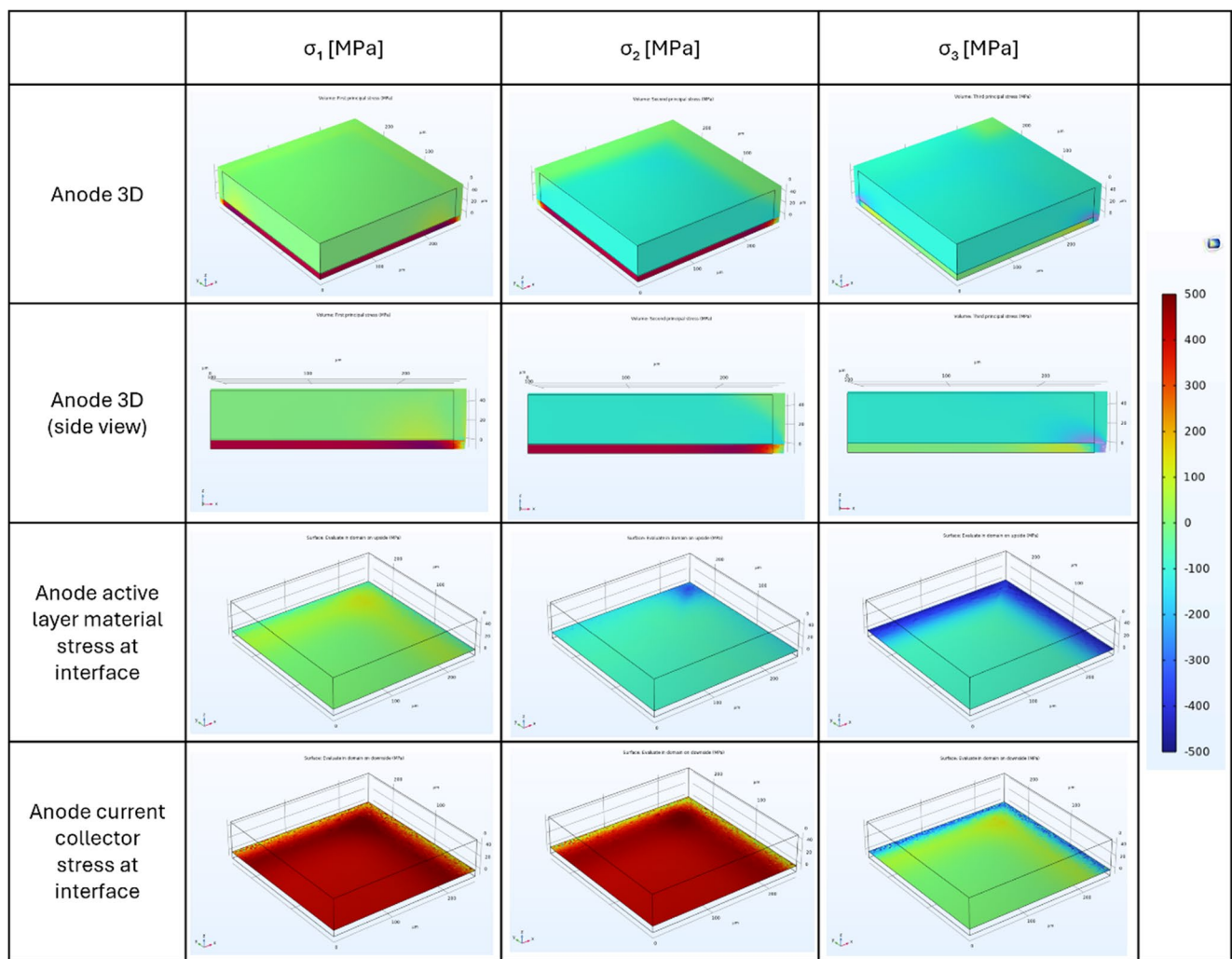


**Fig. 3** Spatial distributions of  $\sigma_1$ ,  $\sigma_2$ ,  $\sigma_3$  with 3D model for expansion of **anode** active material ( $E=2.14$  GPa) during lithiation. Flat current collectors

within the active material exhibit slightly tensile values up to approximately +80 MPa, while the current collector is in compression up to approximately -200 MPa. Values of  $\sigma_3$  remain in compression within the current collector, up to approximately -200 MPa, mirroring  $\sigma_2$ , while the active layer is essentially stress-free, with  $\sigma_3$  close to 0 MPa.

### 3.2 2D model and parametric study

Figures 5 and 6 present the simulated spatial distributions of the three principal stresses ( $\sigma_1$ ,  $\sigma_2$ ,  $\sigma_3$ ) calculated with the 2D model for the same electrodes with flat (untextured) current collectors. A quantitative comparison between results obtained with the 2D and 3D models was carried out to validate the accuracy of the former. Stress values extracted from the 2D model were compared with corresponding results from the 3D model within the central region and at the edges of both electrodes. The analysis

highlighted good agreement between the two models, with deviations consistently below 10%.

For the anode (Fig. 5), values of  $\sigma_1$  within the active material were approximately 0 MPa within the central region with both models, followed by a rise and then return to 0 MPa near the edge. Values of the same parameter within the current collector were +280 MPa in the central region and +150 MPa at the edge with the 2D model, and +300 MPa and +160 MPa, respectively, with the 3D model. Similarly, values of  $\sigma_3$  within the active material were approximately -60 MPa within the central region for both models and -360 MPa and -390 MPa at the edge with the 2D and 3D models, respectively. Within the current collector, values of the same parameter were approximately 0 MPa within the central region and -290 MPa and -300 MPa at the edge with the 2D and 3D models, respectively.

For the cathode (Fig. 6), values of  $\sigma_1$  within the active material were approximately +50 MPa within the central

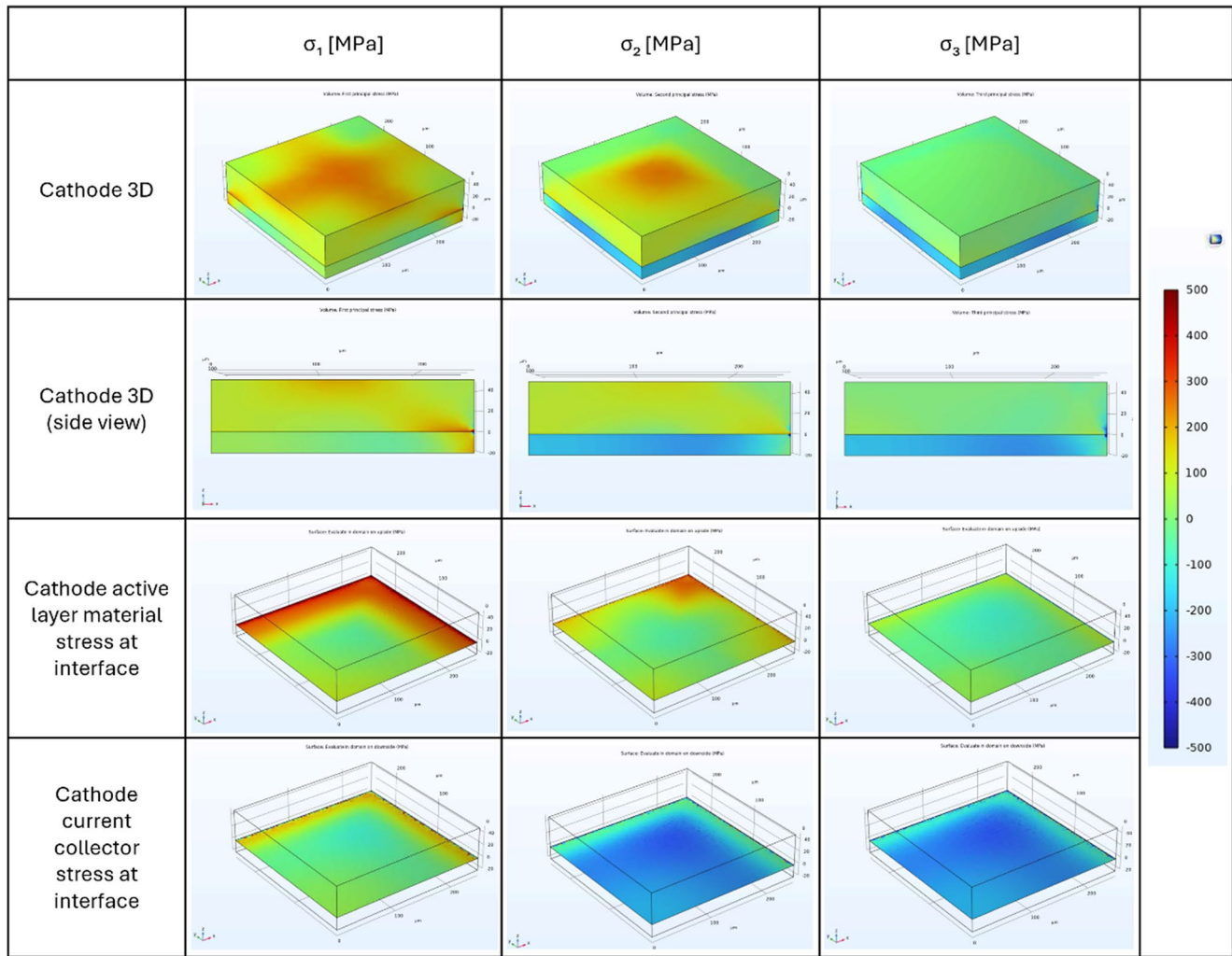


**Fig. 4** Spatial distributions of  $\sigma_1$ ,  $\sigma_2$ ,  $\sigma_3$  with 3D model for contraction of **cathode** active material ( $E=55.0$  GPa) during delithiation. Flat current collectors

region with both models, rising to +400 MPa at the edge with the 2D model and +410 MPa with the 3D model. Values of the same parameter within the current collector were approximately 0 MPa within the central region with both models, rising to +120 MPa at the edge with the 2D model and +130 MPa with the 3D model. Values of  $\sigma_3$  within the active layer were instead 0 MPa within the central region with both models, while values at the edge were  $-340$  MPa with the 2D model and  $-320$  MPa with the 3D model. Values of the same parameter within the current collector reached  $-200$  MPa within the central region with both models, while values at the edge were  $-280$  MPa with the 2D model and  $-310$  MPa with the 3D model.

In contrast to the other principal stresses,  $\sigma_2$  differed significantly between the 2D and 3D models. In the latter case, moderate in-plane tensile or compressive stresses (depending on the electrode) developed due to biaxial restraint, whereas in the 2D model,  $\sigma_2$  was constrained to zero due

to the imposed plane stress condition. This discrepancy did not, however, affect the principal stress components  $\sigma_1$  and  $\sigma_3$ , which were more representative of the stress field. Despite the enforced plane stress condition, the 2D model therefore captured the dominant stress state at the interface with high fidelity, validating its use for subsequent parametric studies assessing stress within laser-textured electrodes.

Laser texturing of the current collector led to significant changes in the developed stresses during cycling. An example of the resulting stress distribution within the anode is shown in Figs. 7 and 8 ( $\lambda=6$   $\mu\text{m}$ ,  $H/\lambda=1$  and  $E=2.14$  GPa). The results are presented within the undeformed material volume to facilitate interpretation. Figure 7a presents the spatial distribution of the first principal stress ( $\sigma_1$ ) within the active layer. As for the anode with a flat current collector, values of  $\sigma_1$  are essentially zero within the bulk material as the expanding active layer is mechanically constrained by the current collector, inhibiting free dilation and

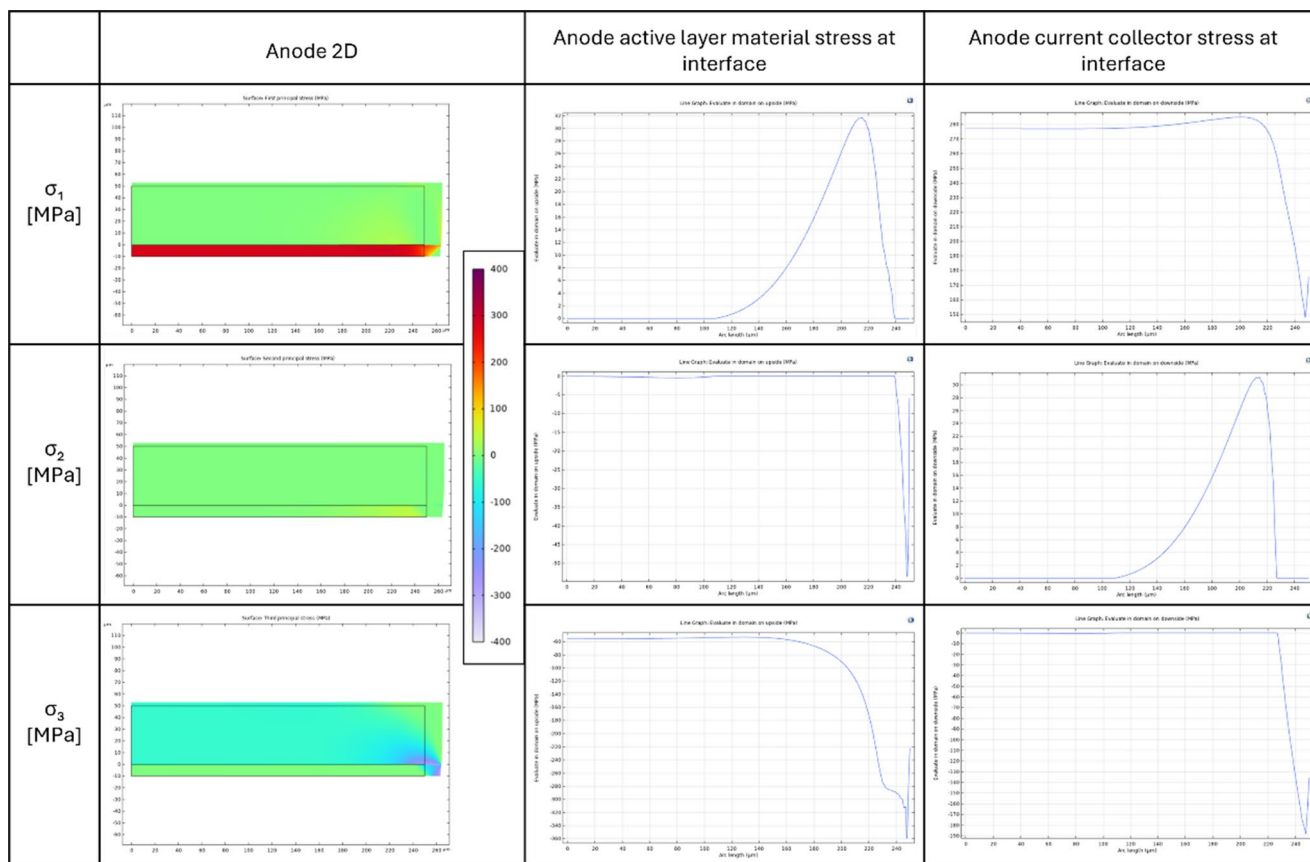


**Fig. 5** Spatial distributions of  $\sigma_1$ ,  $\sigma_2$ ,  $\sigma_3$  with 2D model for expansion of **anode** active material ( $E=2.14$  GPa) during lithiation. Flat current collector

thereby inducing compressive stress within the active material. Stress concentration near the interface with the current collector instead leads to relatively high tensile values of  $\sigma_1$  within the deepest regions of the surface topography, as deformation of the current collector, and consequently also the active layer, exceeds the natural volumetric expansion of the latter. Figure 7b shows the corresponding profile of  $\sigma_1$  along the interface with the current collector, highlighting the effect of laser texturing on stress concentration. Two distinct regions emerge, including a central zone exhibiting nearly constant peak stresses, adjacent to the symmetry boundary, and an edge region where peak values vary more significantly. By comparing  $\sigma_1$  for the active material in Fig. 5 (flat current collector) with the same parameter in Fig. 7b (laser-textured current collector), it can be observed that laser texturing has no significant influence on the extension of edge effects. The central zone was therefore considered representative of real electrodes, typically several  $\text{cm}^2$  in area, as edge regions were of limited extension ( $<150 \mu\text{m}$ ).

Figure 8a presents the spatial distribution of the Von Mises stress ( $\sigma_v$ ) within the current collector for the same electrode, while Fig. 8b shows the corresponding profile

along the interface with the active material. The current collector is subject to tensile stresses within the bulk material due to expansion of the active material, with some stress concentration observed at the interface. As with the active material, stress concentration effects induced by laser texturing are superimposed on the stress profile obtained with the flat current collector, while texturing does not significantly influence the extension of edge effects. This outcome again confirms that the surface topography leads to local stress concentration within both the active layer and current collector.

Figures 9 and 10 illustrate the evolution of the first principal stress ( $\sigma_1$ ) within the active material and Von Mises stress ( $\sigma_v$ ) within the current collector of the cathode ( $\lambda=6 \mu\text{m}$ ,  $H/\lambda=1$  and  $E=55.0$  GPa). Values of  $\sigma_1$  within the active material (Fig. 9a) are slightly tensile throughout the bulk volume as the current collector constrains its volumetric contraction. Figure 9b shows the  $\sigma_1$  profile at the interface with the current collector, where peaks coincide with the deepest regions of the surface topography. Figure 10a focuses on the current collector, where values of  $\sigma_v$  remain exclusively positive due to the compressive action of the active material. Again, a clear correlation can be observed

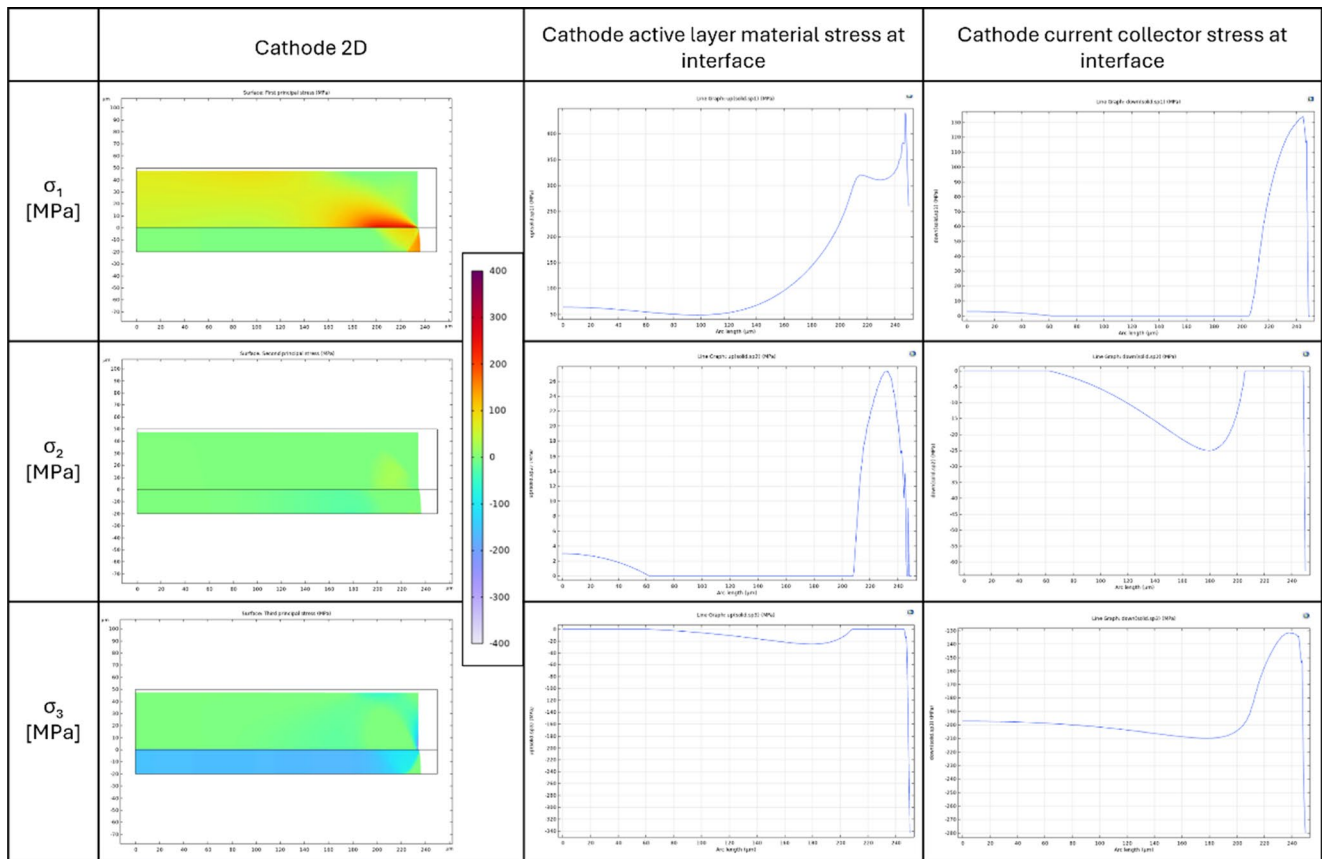


**Fig. 6** Spatial distributions of  $\sigma_1$ ,  $\sigma_2$ ,  $\sigma_3$  with 2D model for contraction of **cathode** active material ( $E=55.0$  GPa) during delithiation. Flat current collector

between interface stress peaks in Fig. 10b and laser-textured valleys, confirming that surface topography drives local stress concentration at the interface between the current collector and active material.

Figures 11 and 12 summarize the results of the parametric study performed with the 2D model. For each electrode, peak values of the first principal stress ( $\sigma_1$ ) within the central zone of the active material, Von Mises stress ( $\sigma_v$ ) within the current collector and normal ( $p$ ) and shear ( $\tau$ ) contact pressures at the interface between the two materials are presented as functions of the period ( $\lambda$ ) and aspect ratio ( $H/\lambda$ ) of the laser-textured surface topography and Young's modulus ( $E$ ) of the active material (derived from the porosity as per Table 3). The anode with flat (untextured) current collector exhibited values of around  $\sigma_1=0$  MPa within the active material,  $\sigma_v=+275$  MPa within the current collector and  $p=0$  MPa and  $\tau=0$  MPa at the interface between the two ( $E=2.14$  GPa). The cathode with flat (untextured) current collector instead exhibited values of  $\sigma_1=+90$  MPa,  $\sigma_v=+200$  MPa,  $p=0$  MPa and  $\tau=0$  MPa ( $E=55.0$  GPa). Due to the relative lower dependence of all stress values on the period of the surface topography and Young's modulus of the active material, only results relating to minimum

and maximum values of these parameters are presented in Figs. 11 and 12 for clarity. Complete data for all simulations are available in the Supplementary Material.

Peak values of  $\sigma_1$  within the central zone of the anode active material (Fig. 11a) increase by approximately one order of magnitude with increases in the aspect ratio of the current collector surface topography over the considered range, with the trend approaching asymptotic behavior for aspect ratios close to  $H/\lambda=1$ . In contrast, the period has negligible influence, with minimal changes in  $\sigma_1$  between  $\lambda=1$   $\mu\text{m}$  and  $\lambda=10$   $\mu\text{m}$ . The Young's modulus of the active material, a function of its porosity (Table 3), has a moderate impact on  $\sigma_1$  over the considered range, but to a lesser extent than the aspect ratio. Increases in Young's modulus, or decreases in porosity, lead to increases in  $\sigma_1$ , as the higher stiffness of the active material leads to greater tensile stresses during expansion. Similar considerations apply to peak normal and tangential contact pressures at the interface between the current collector and active material (Fig. 11c-d), while slightly less marked increases in the Von Mises stress within the copper current collector can be observed (Fig. 11b). Again, the aspect ratio is the dominant factor, with higher aspect ratios leading to significantly higher

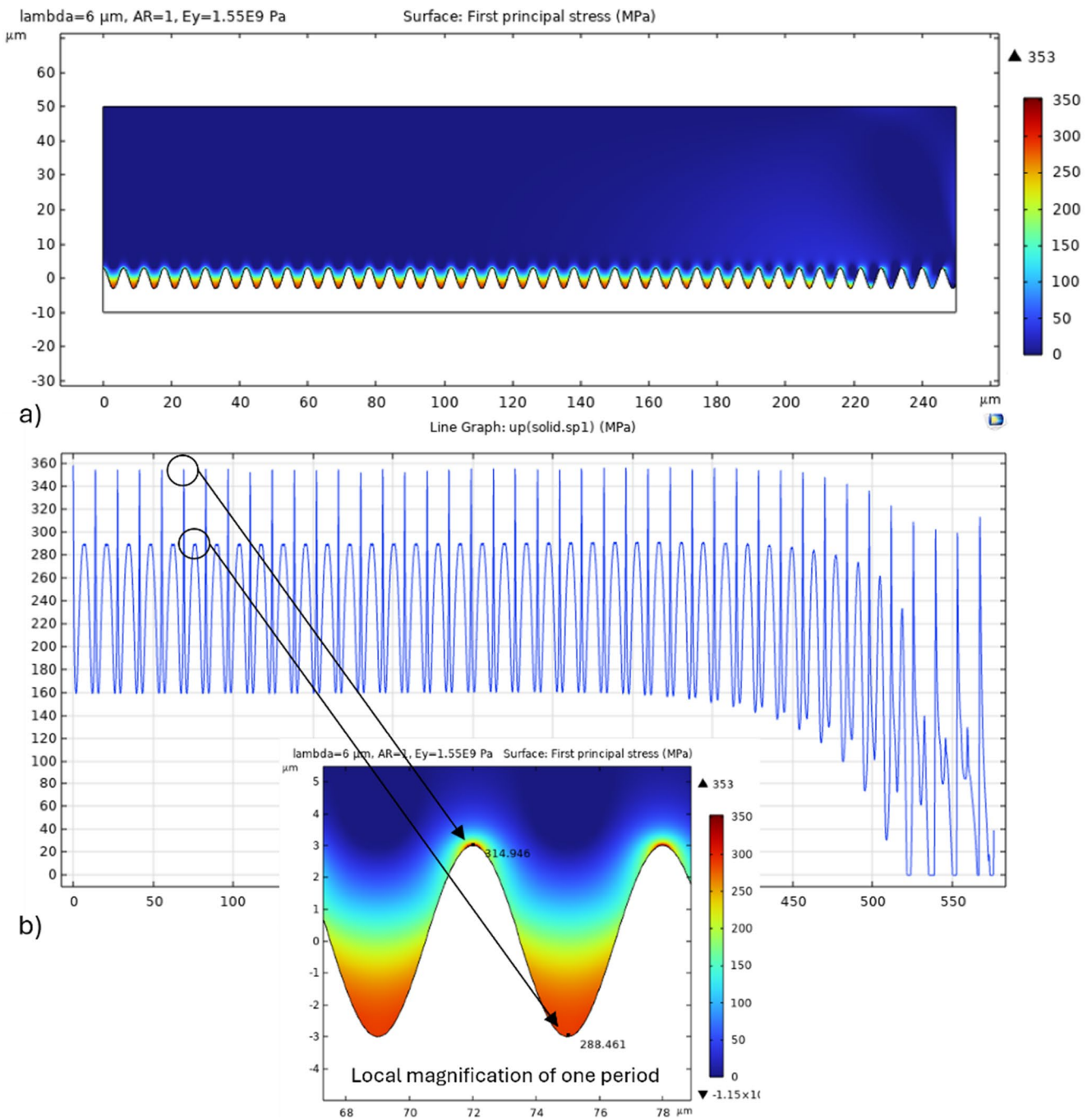


**Fig. 7** First principal stress ( $\sigma_1$ ) within **anode** active layer ( $E=1.55$  GPa): (a) spatial distribution, (b) value at interface with current collector. Laser-textured current collector with  $\lambda=6$   $\mu\text{m}$ ,  $H/\lambda=1$

stresses, while the influence of the laser period is negligible. These outcomes imply intermediate stress values in all cases for LIPSS, where the aspect ratio is typically in the range 0.3–0.6, and dependence on the laser pulse fluence and number of pulses for DLIP, where the aspect ratio can vary within the range 0–1 depending on the quantity of ablated material. The Young’s modulus of the active material instead has a moderate influence on the Von Mises stress

within the current collector and shear contact pressure, particularly at high aspect ratios.

The aspect ratio again has a significant impact on all stress components within the cathode (Fig. 12), with large increases in all parameters from  $H/\lambda=0.1$  to  $H/\lambda=1$ . In this case, the period has minimal impact, while the Young’s modulus of the active material has very little impact on peak values of  $\sigma_1$  within the central zone of the active material

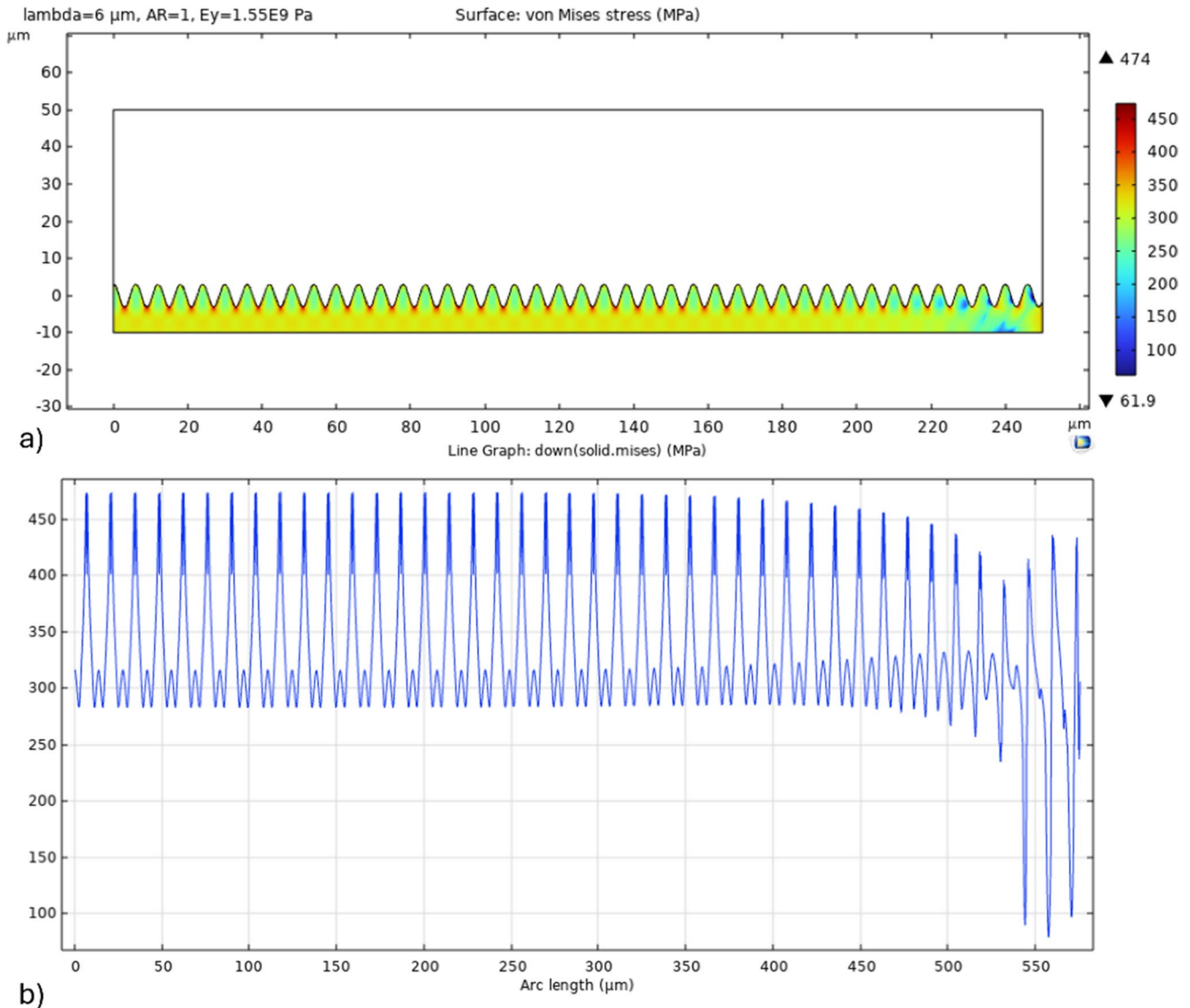


**Fig. 8** Von Mises stress ( $\sigma_v$ ) within **anode** current collector: **(a)** spatial distribution, **(b)** value at interface with active layer. Laser-textured current collector with  $\lambda=6 \mu\text{m}$ ,  $H/\lambda=1$

and no detectable impact on the other parameters which are therefore represented by the same curve in Fig. 12b-d. As for the cathode, outcomes imply intermediate stress values in all cases for LIPSS, and dependence on laser pulse fluence and the number of pulses for DLIP.

When comparing the stress distributions shown in Fig. 11 for expansion of the anode to those shown in Fig. 12 for contraction of the cathode, it is clear that the active material behaves fundamentally differently within the two electrodes due to the type of volumetric change taking place (expansion versus contraction) and Young's Modulus of the active materials. Higher peak values of the first principal stress ( $\sigma_1$ ) develop within the central zone of the cathode active material as the current collector restricts material contraction, which when combined with the relatively high

Young's Modulus of the former, generates high peak tensile values of  $\sigma_1$ . Values of the same parameter are somewhat lower within the anode active material due to both the lower Young's Modulus and compressive state of the layer during expansion, leading to tensile values of  $\sigma_1$  only within regions subject to specific stress concentration effects. Higher peak values of Von Mises stress ( $\sigma_v$ ) develop within the anode current collector due to the greater volumetric expansion of the anode (28%) than contraction of the cathode (10%). Normal ( $p$ ) and shear ( $\tau$ ) contact pressures at the interface between the active material and current collector also differ between the two electrodes. The anode exhibits elevated normal contact pressure at the interface under expansion, whereas the cathode shows more pronounced shear stress under compression. Changes in the Young's

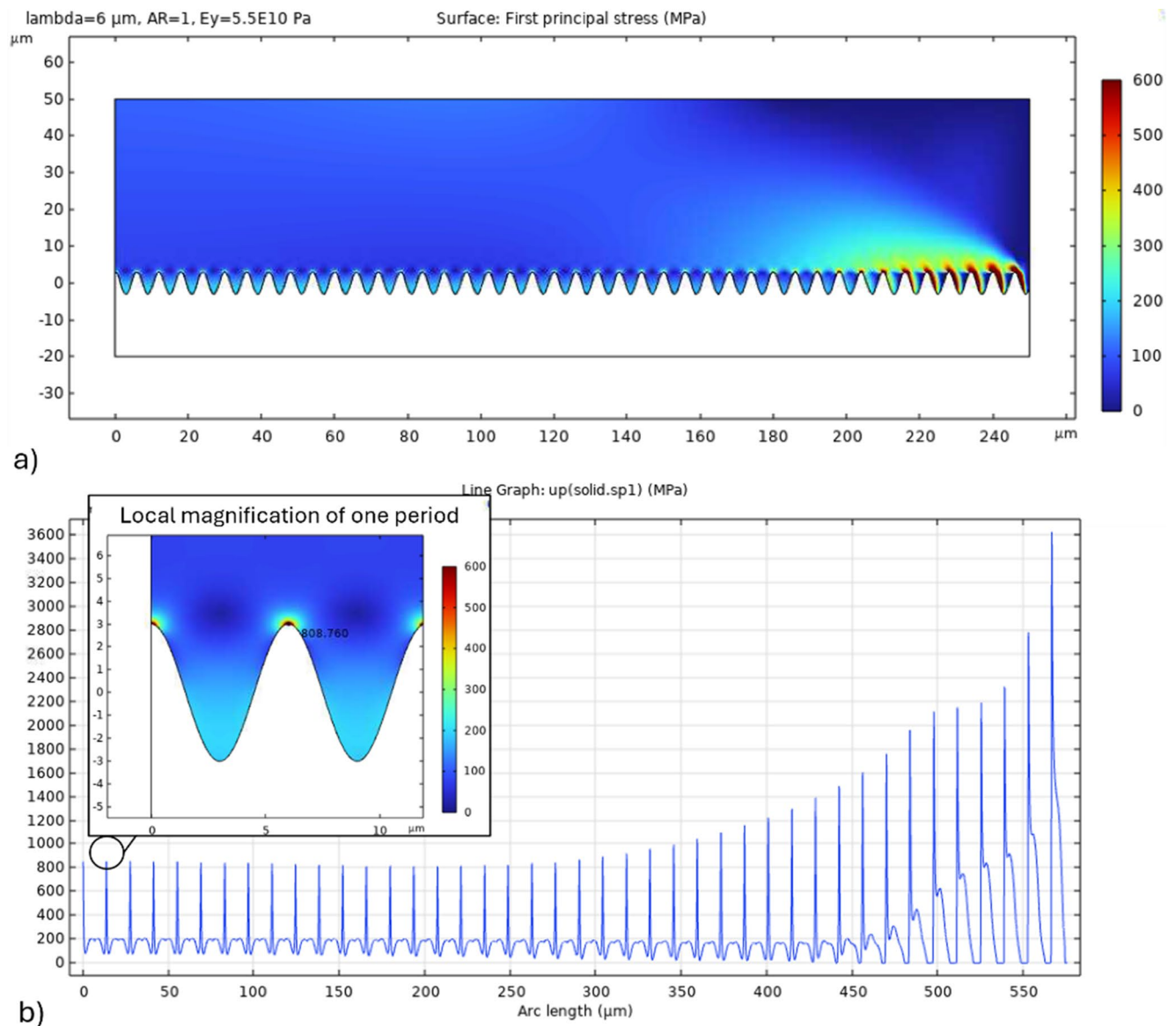


**Fig. 9** First principal stress ( $\sigma_1$ ) within **cathode** active layer ( $E=55.0$  GPa): **(a)** spatial distribution, **(b)** value at interface with current collector. Laser-textured current collector with  $\lambda=6$   $\mu\text{m}$ ,  $H/\lambda=1$

modulus of the active material, a function of its porosity (Table 3), also affect how stresses develop for the anode, whereas this property appears to play a negligible role for the cathode. This outcome is likely due to the lower stiffness of the active material in the anode, leading to greater sensitivity to changes in Young's modulus or porosity. For both electrodes, changes in the texture period have only a modest impact, while increases in the aspect ratio consistently lead to greater stress concentration.

With the aspect ratio of the surface texture being the primary driver of increases in mechanical stresses within Li-ion battery electrodes with laser-textured current collectors, it is worth considering the effects of this parameter on the increase in interface area between the current collector

and active material, which is generally considered to be the main contributor to improving adhesion between the two. Figure 13 presents the theoretical increase in interface area between the current collector and active material for surface topographies considered within simulations (Eq. (2)) as a function of the aspect ratio, assuming complete contact between the two. It must be noted that the theoretical value does not depend on the period nor the mechanical properties of the electrode materials themselves. By comparing the results of the 2D parametric study (Figs. 11 and 12) with the variation in interface area (Fig. 13), it is clear that selection of laser parameters to achieve a given surface topography must be a compromise between improving adhesion between the current collector and active material,

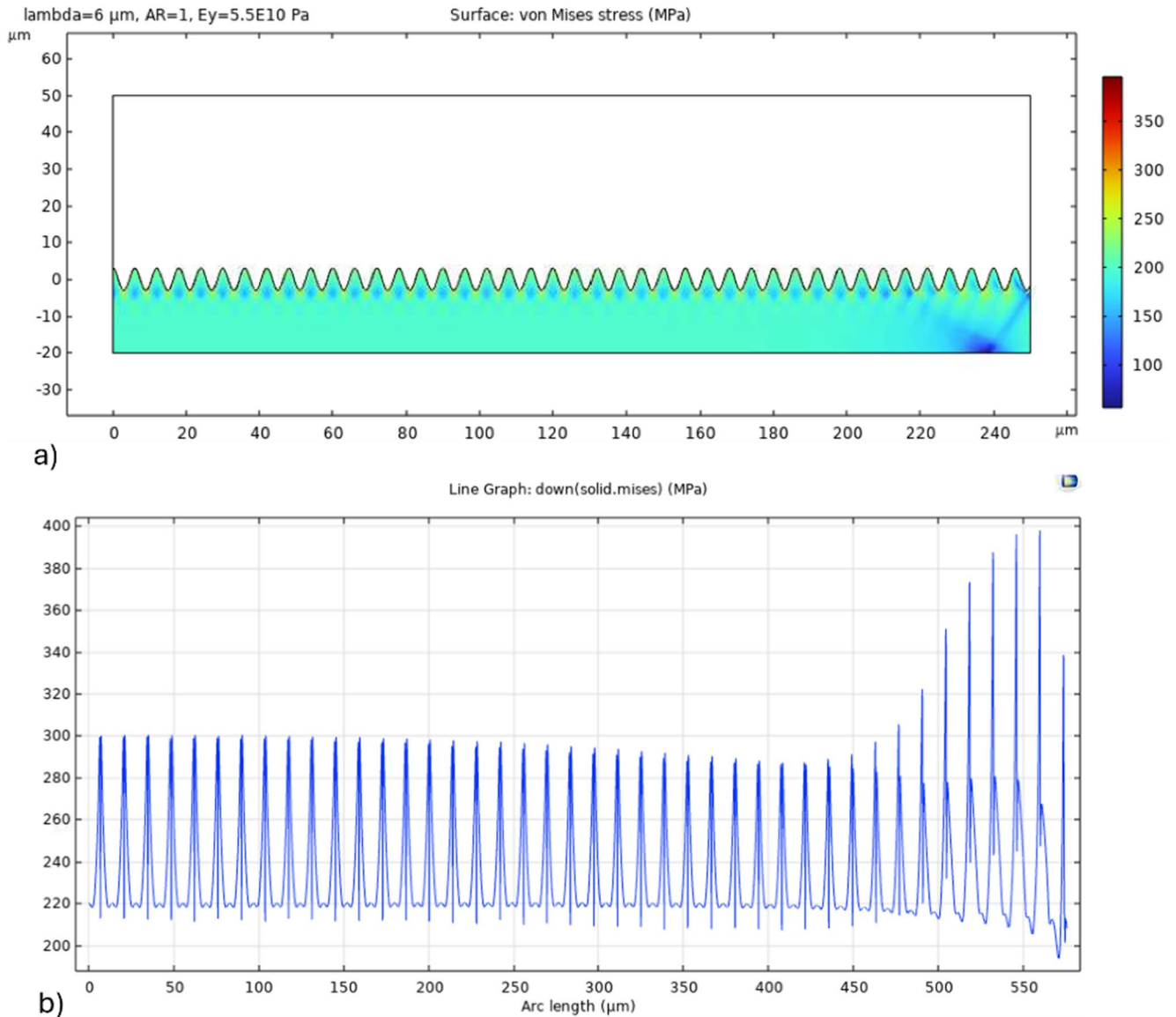


**Fig. 10** Von Mises stress ( $\sigma_v$ ) within **cathode** current collector: **(a)** spatial distribution, **(b)** value at interface with active layer. Laser-textured current collector with  $\lambda=6 \mu\text{m}$ ,  $H/\lambda=1$

and limiting mechanical stresses at and near the interface between the two during cycling. The optimal aspect ratio is therefore the minimum value necessary to inhibit adhesive detachment of the active layer from the current collector via an increase in interface area without promoting cohesive failure of the material during cycling due to stress concentration. Future experimental work is now required to develop a standardized methodology for identifying this optimal condition for specific electrode materials. Outcomes of the investigation nonetheless suggest that both LIPSS and DLIP are potential candidates for laser texturing of Li-ion battery current collectors. The former exhibits advantages in terms of reduced complexity and higher throughput, while the latter instead provides greater flexibility in tailoring the

aspect ratio outside the typical range of 0.4–0.6 achieved with LIPSS.

## 4 Conclusion

The present study has systematically assessed the effects of laser texturing on mechanical stresses within composite silicon-graphite and LNMO Li-ion battery electrodes due to volumetric expansion of the anode and contraction of the cathode during cycling. After comparing the results of 2D and 3D models for flat (untextured) current collectors, the surface topography of ultrashort pulsed laser-textured current collectors was represented with ideal sinusoidal

### ANODE

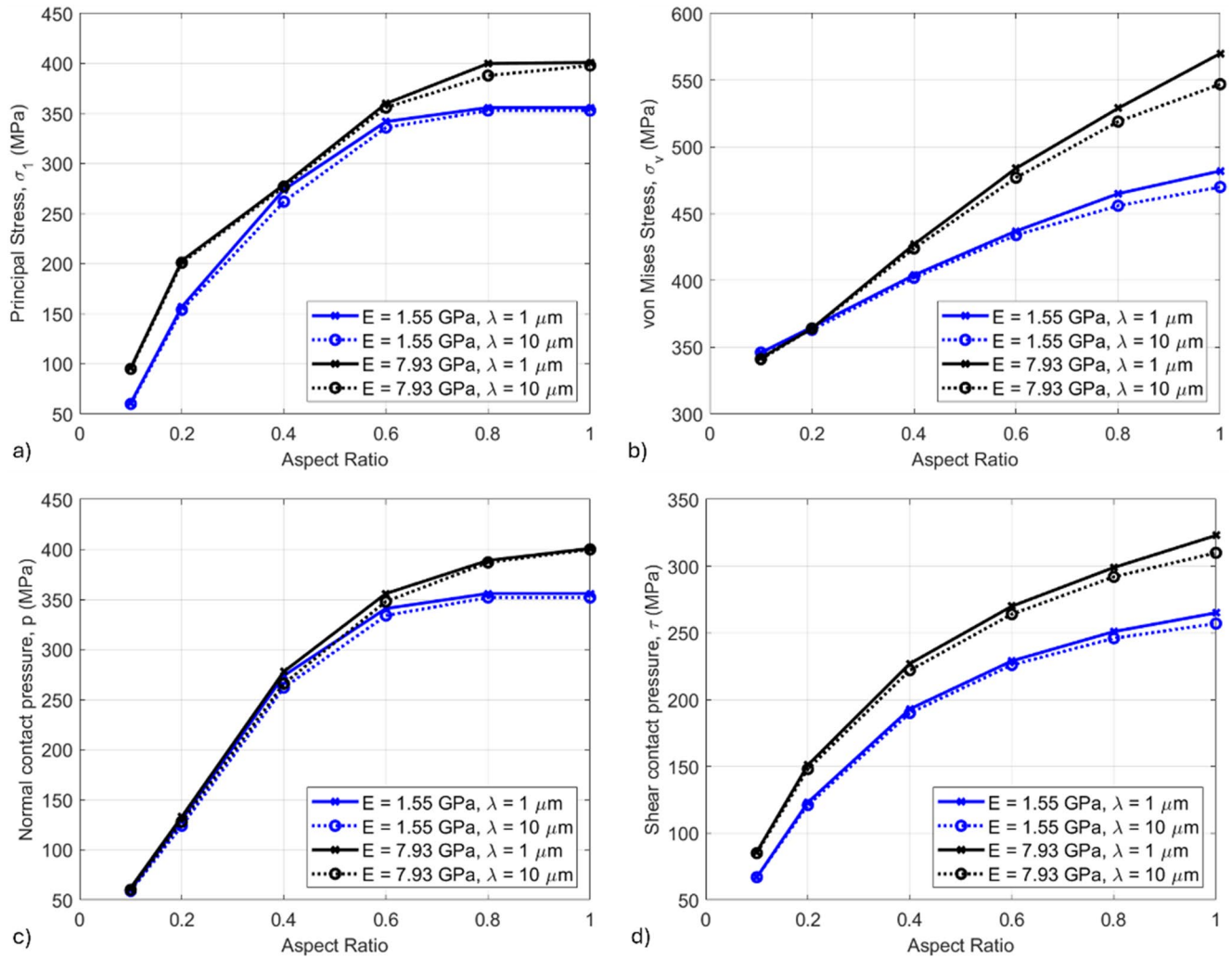


**Fig. 11** Peak mechanical stresses in central zone of **anode** as functions of the period ( $\lambda$ ) and aspect ratio ( $H/\lambda$ ) of laser-textured current collector surface topography and Young's modulus ( $E$ ) of active material: **(a)** First principal stress ( $\sigma_1$ ) within active material, **(b)** Von Mises

stress within current collector, **(c)** normal contact pressure at interface between current collector and active material, **(d)** shear contact pressure at interface between current collector and active material

geometry, allowing a 2D parametric study to be carried out by varying the texture period ( $\lambda$ ) and aspect ratio ( $H/\lambda$ ), as well as the Young's modulus of the active material ( $E$ ), a function of its porosity, over realistic ranges. While representing the surface geometry in this way inevitably led to deviations between simulated and actual stress states, this approach was adopted to consider as wide a range of surface topographies as possible while ensuring a sufficiently large simulation domain to accurately represent the central zone of electrodes.

The results indicated that stress concentration at and near the interface between the current collector and active material led to increases in peak values of the first principal stress ( $\sigma_1$ ) within the central zone of the active material, considered indicative of the likelihood of brittle failure of

this element, the Von Mises stress ( $\sigma_v$ ) within the current collector, considered indicative of the likelihood of ductile failure of this element, and the normal ( $p$ ) and shear ( $\tau$ ) contact pressures at the interface between the two materials, considered indicative of electrode failure due to adhesion issues. All peak stress values increased with the aspect ratio of the surface texture, with little or no dependence on the period. These outcomes imply intermediate stress values in all cases for LIPSS, and dependence on laser pulse fluence and the number of pulses for DLIP. Increases in the Young's modulus of the active material, or decreases in its porosity, also led to moderate increases in all stress values in most cases.

Increasing the aspect ratio of the surface texture leads to an increase in the interfacial area between the current

## CATHODE

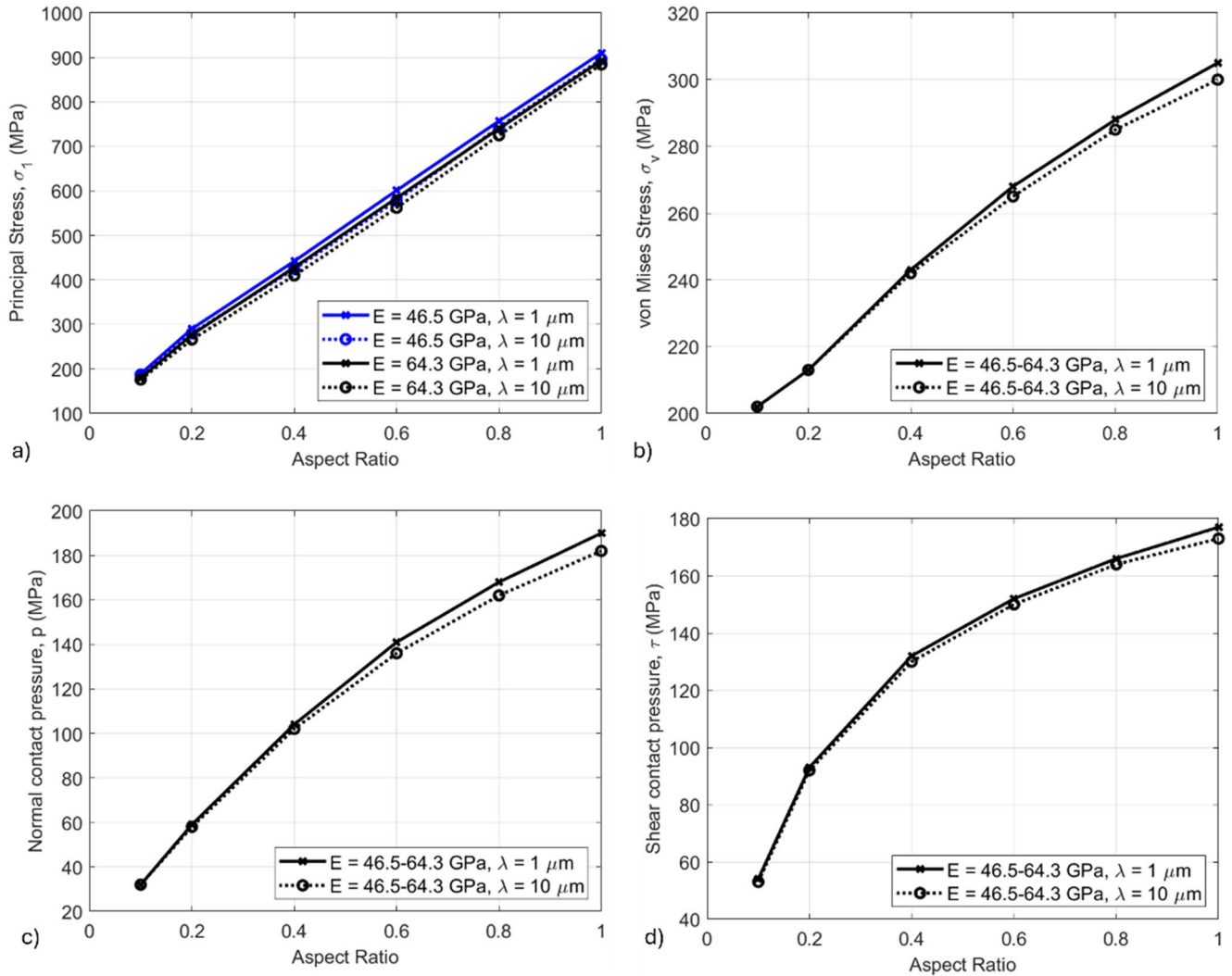


**Fig. 12** Peak mechanical stresses in central zone of **cathode** as functions of the period ( $\lambda$ ) and aspect ratio ( $H/\lambda$ ) of laser-textured current collector surface topography and Young's modulus ( $E$ ) of active material: **(a)** First principal stress ( $\sigma_1$ ) within active material, **(b)** Von Mises

stress within current collector, **(c)** normal contact pressure at interface between current collector and active material, **(d)** shear contact pressure at interface between current collector and active material

collector and active material, which can provide benefits in terms of adhesion between the two, and therefore lifespan of a given cell; however, the results of the present study clearly show that a higher aspect ratio leads to greater peak stresses, which may cause deformation, failure or delamination at the interface. While only the first charge cycle was modeled, trends can be expected to also apply to subsequent cycles as the underlying driver of stress concentration would continue to be present to some degree. Despite these outcomes, there is currently a lack of experimental evidence specifically associating stress concentration due to current collector topography with the electrochemical performance of electrodes during cycling. As such, stress

values should be evaluated in conjunction with other factors such as increases in surface area, binder quality and the mechanical properties of electrode materials. The present study nonetheless provides quantitative insight into the effects of different combinations of geometric parameters on mechanical stresses experience by electrodes, clearly highlighting the need for additional experimental investigation into the performance of electrodes subject to various surface treatments. Such conclusions go beyond laser texturing itself and can be broadly applied to all surface texturing methods. Further studies are now required to provide stronger experimental data correlating stress states within electrodes with their electrochemical performance over a

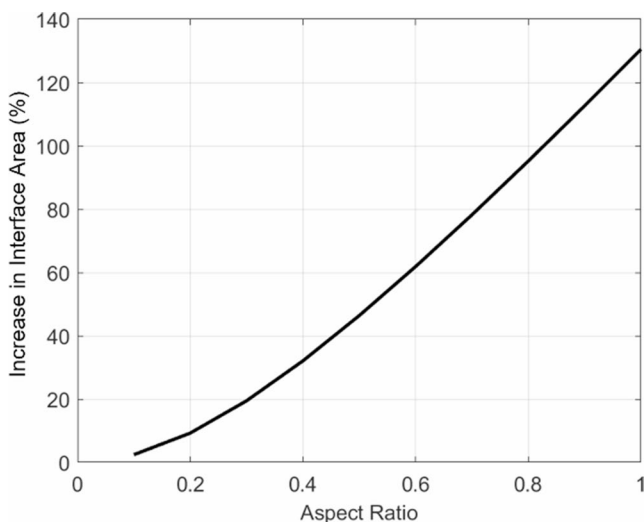


**Fig. 13** Theoretical increase in interface area between current collector and active material as a function of the aspect ratio ( $H/\lambda$ ) of laser-textured surface topography

larger number of cycles. Additional simulations must also be performed with more complex geometries achieved via ultrashort pulsed laser irradiation, including 3D models accounting for hierarchical surface structures and the presence of residual byproducts after laser processing. Finally, failure mechanisms must be introduced within simulations, together with cumulative stress affects over multiple cycles, to provide insight into mechanically-induced cell degradation and capacity fade, providing additional steps towards mitigating this phenomenon.

**Acknowledgements** The authors kindly acknowledge financial support received from the GIGAGREEN project (Horizon Europe, grant agreement No. 101069707).

**Funding** Open access funding provided by Università degli Studi di Parma within the CRUI-CARE Agreement.

## Declarations

**Competing interest** The authors declare that they have no known competing financial interests or personal relationships that could have appeared to influence the work reported in this paper.

**Open Access** This article is licensed under a Creative Commons Attribution 4.0 International License, which permits use, sharing, adaptation, distribution and reproduction in any medium or format, as long as you give appropriate credit to the original author(s) and the source, provide a link to the Creative Commons licence, and indicate if changes were made. The images or other third party material in this article are included in the article's Creative Commons licence, unless indicated otherwise in a credit line to the material. If material is not included in the article's Creative Commons licence and your intended use is not permitted by statutory regulation or exceeds the permitted use, you will need to obtain permission directly from the copyright holder. To view a copy of this licence, visit <http://creativecommons.org/licenses/by/4.0/>.

## References

- Kittner N, Lill F, Kammen DM (2017) Energy storage deployment and innovation for the clean energy transition. *Nat Energy* 2:17125. <https://doi.org/10.1038/energy.2017.125>
- Frith JT, Lacey MJ, Ulissi U (2023) A non-academic perspective on the future of lithium-based batteries. *Nat Commun* 14:420. <https://doi.org/10.1038/s41467-023-35933-2>
- Hasan MK, Mahmud M, Habib A.K.M. Ahasan, Motakabber SMA, Islam S (2021) Review of electric vehicle energy storage and management system: standards, issues, and challenges. *J Energy Storage* 41:102940. <https://doi.org/10.1016/j.est.2021.102940>
- Liang G, Peterson VK, See KW, Guo Z, Pang WK (2020) Developing high-voltage spinel  $\text{LiNi}_{0.5}\text{Mn}_{1.5}\text{O}_4$  cathodes for high-energy-density lithium-ion batteries: current achievements and future prospects. *J Mater Chem A* 8:15373–15398. <https://doi.org/10.1039/D0TA02812F>
- Li P, Kim H, Myung S-T, Sun Y-K (2021) Diverting exploration of silicon anode into practical way: a review focused on silicon-Graphite composite for lithium ion batteries. *Energy Storage Mater* 35:550–576. <https://doi.org/10.1016/j.ensm.2020.11.028>
- Dühnen S, Betz J, Kolek M, Schmuch R, Winter M, Placke T (2020) Toward green battery cells: perspective on materials and technologies. *Small Methods* 4:2000039. <https://doi.org/10.1002/smt.202000039>
- Kabir MM, Demirocak DE (2017) Degradation mechanisms in Li-ion batteries: a state-of-the-art review: degradation mechanisms in Li-ion batteries: A State-of-the-Art review. *Int J Energy Res* 41:1963–1986. <https://doi.org/10.1002/er.3762>
- Guo L, Thornton DB, Koronfel MA, Stephens IEL, Ryan MP (2021) Degradation in lithium ion battery current collectors. *J Phys Energy* 3:032015. <https://doi.org/10.1088/2515-7655/ac0c04>
- Guo R, Zhang S, Ying H, Yang W, Wang J, Han W-Q (2019) New, effective, and low-cost dual-functional binder for porous silicon anodes in lithium-ion batteries. *ACS Appl Mater Interfaces* 11:14051–14058. <https://doi.org/10.1021/acsami.8b21936>
- Yoon S, Jang H-S, Kim S, Kim J, Cho KY (2017) Crater-like architectural aluminum current collectors with superior electrochemical performance for Li-ion batteries. *J Electroanal Chem* 797:37–41. <https://doi.org/10.1016/j.jelechem.2017.05.017>
- Wang R, Li W, Liu L, Qian Y, Liu F, Chen M, Guo Y, Liu L (2019) Carbon black/graphene-modified aluminum foil cathode current collectors for lithium ion batteries with enhanced electrochemical performances. *J Electroanal Chem* 833:63–69. <https://doi.org/10.1016/j.jelechem.2018.11.007>
- Yang Y, Yuan W, Zhang X, Ke Y, Qiu Z, Luo J, Tang Y, Wang C, Yuan Y, Huang Y (2020) A review on structuralized current collectors for high-performance lithium-ion battery anodes. *Appl Energy* 276:115464. <https://doi.org/10.1016/j.apenergy.2020.115464>
- Onsrud M, Tezel AO, Fotedar S, Svensson AM (2022) Novel carbon coating on aluminum current collectors for lithium-ion batteries. *SN Appl Sci* 4:225. <https://doi.org/10.1007/s42452-022-05103-y>
- Romoli L, Lutey AHA, Lazzini G (2022) Laser texturing of Li-ion battery electrode current collectors for improved active layer interface adhesion. *CIRP Ann* 71:481–484. <https://doi.org/10.1016/j.cirp.2022.04.034>
- Wang Y, Zhao Z, Zhong J, Wang T, Wang L, Xu H, Cao J, Li J, Zhang G, Fei H, Zhu J (2022) Hierarchically micro/nanostructured current collectors induced by ultrafast femtosecond laser strategy for high-performance lithium-ion batteries. *ENERGY Environ Mater* 5:969–976. <https://doi.org/10.1002/eem2.12223>

16. Tallone P, Spriano S, Versaci D, Ferraris S, Tori A, Bodoardo S (2024) Picosecond laser texturing of Al current collector to improve cycling performances and simplify recycling of lithium-ion batteries. *Surfaces and Interfaces* 51:104659. <https://doi.org/10.1016/j.surfin.2024.104659>
17. Ravesio E, Montinaro G, Mincuzzi G, Negozio M, Versaci D, Gartiser V, Lutey AHA, Bella F, Bodoardo S (2025) Ultrashort pulsed laser texturing of current collector for Si/C Li-ion anodes: characterization of electrochemical performance and evolution of interface morphology. *J Energy Storage* 109:115226. <https://doi.org/10.1016/j.est.2024.115226>
18. Lorazo P, Lewis LJ, Meunier M (2006) Thermodynamic pathways to melting, ablation, and solidification in absorbing solids under pulsed laser irradiation. *Phys Rev B* 73:134108
19. Porneala C, Willis DA (2009) Time-resolved dynamics of nanosecond laser-induced phase explosion. *J Phys Appl Phys* 42:155503
20. Lutey AHA, Negozio M, Ravesio E, Versaci D (2025) Characterization of adhesion in Lithium-Ion battery electrodes with laser-textured current collectors. *J Manuf Sci Eng* 147:071006. <https://doi.org/10.1115/1.4068239>
21. Bonse J, Krüger J, Höhm S, Rosenfeld A (2012) Femtosecond laser-induced periodic surface structures. *J Laser Appl* 24:042006. <https://doi.org/10.2351/1.4712658>
22. Gnilitzki I, Derrien TJ-Y, Levy Y, Bulgakova NM, Mocek T, Orazi L (2017) High-speed manufacturing of highly regular femtosecond laser-induced periodic surface structures: physical origin of regularity. *Sci Rep* 7:8485
23. Hou M, Zhong Y, Zhang J, Xie B, Lai S, Dong S, Chen Y, Chen X (2025) Femtosecond Bessel laser beam induced concentric rings on SiC for circular symmetry wide-viewing angle structural color. *Opt Laser Technol* 181:111813. <https://doi.org/10.1016/j.optlastec.2024.111813>
24. Lutey AHA, Gemini L, Romoli L, Lazzini G, Fuso F, Faucon M, Kling R (2018) Towards laser-textured antibacterial surfaces. *Sci Rep* 8:10112. <https://doi.org/10.1038/s41598-018-28454-2>
25. Fraggelakis F, Mincuzzi G, Lopez J, Manek-Hönninger I, Kling R (2019) Controlling 2D laser nano structuring over large area with double femtosecond pulses. *Appl Surf Sci* 470:677–686. <https://doi.org/10.1016/j.apsusc.2018.11.106>
26. Tsididis GD, Fotakis C, Stratakis E (2015) From ripples to spikes: a hydrodynamical mechanism to interpret femtosecond laser-induced self-assembled structures. *Phys Rev B*. <https://doi.org/10.1103/PhysRevB.92.041405>
27. Mincuzzi G, Gemini L, Faucon M, Kling R (2016) Extending ultra-short pulse laser texturing over large area. *Appl Surf Sci* 386:65–71. <https://doi.org/10.1016/j.apsusc.2016.05.172>
28. Müller DW, Fox T, Grützmacher PG, Suarez S, Mücklich F (2020) Applying ultrashort pulsed direct laser interference patterning for functional surfaces. *Sci Rep* 10:3647. <https://doi.org/10.1038/s41598-020-60592-4>
29. Weber R, Graf T, Berger P, Onuseit V, Wiedenmann M, Freitag C, Feuer A (2014) Heat accumulation during pulsed laser materials processing. *Opt Express* 22:11312. <https://doi.org/10.1364/OE.22.011312>
30. Martan J, Prokešová L, Moskal D, Ferreira De Faria BC, Honner M, Lang V (2021) Heat accumulation temperature measurement in ultrashort pulse laser micromachining. *Int J Heat Mass Transf* 168:120866. <https://doi.org/10.1016/j.ijheatmasstransfer.2020.12.0866>
31. Christensen J (2010) Modeling diffusion-induced stress in Li-Ion cells with porous electrodes. *J Electrochem Soc* 157:A366. <https://doi.org/10.1149/1.3269995>
32. Mukhopadhyay A, Sheldon BW (2014) Deformation and stress in electrode materials for Li-ion batteries. *Prog Mater Sci* 63:58–116. <https://doi.org/10.1016/j.pmatsci.2014.02.001>
33. Xu R, Zhao K (2016) Electrochemomechanics of electrodes in Li-Ion batteries: a review. *J Electrochem Energy Convers Storage* 13:030803. <https://doi.org/10.1115/1.4035310>
34. Banerjee J, Dutta K (2017) Materials for electrodes of Li-Ion batteries: issues related to stress development. *Crit Rev Solid State Mater Sci* 42:218–238. <https://doi.org/10.1080/10408436.2016.1173011>
35. Jangid MK, Mukhopadhyay A (2019) Real-time monitoring of stress development during electrochemical cycling of electrode materials for Li-ion batteries: overview and perspectives. *J Mater Chem A* 7:23679–23726. <https://doi.org/10.1039/C9TA06474E>
36. Rabczuk T (2013) Computational methods for fracture in brittle and quasi-brittle solids: state-of-the-art review and future perspectives. *ISRN Appl Math* 2013:1–38. <https://doi.org/10.1155/2013/849231>
37. Wang Y-Z, Li G-Q, Wang Y-B, Lyu Y-F (2021) Simplified method to identify full von Mises stress-strain curve of structural metals. *J Constr Steel Res* 181:106624. <https://doi.org/10.1016/j.jcsr.2021.106624>
38. Luo H, Zhu J, Sahraei E, Xia Y (2018) Adhesion strength of the cathode in lithium-ion batteries under combined tension/shear loadings. *RSC Adv* 8:3996–4005. <https://doi.org/10.1039/C7RA12382E>
39. Zhu HX, Fan TX, Zhang D (2015) Composite materials with enhanced dimensionless young's modulus and desired poisson's ratio. *Sci Rep* 5:14103. <https://doi.org/10.1038/srep14103>
40. Kováčik J (1999) Correlation between young's modulus and porosity in porous materials. *J Mater Sci Lett* 18:1007–1010. <http://doi.org/10.1023/A:1006669914946>
41. Phani KK, Niyogi SK (1987) Young's modulus of porous brittle solids. *J Mater Sci* 22:257–263. <https://doi.org/10.1007/BF01160581>
42. Hfaiedh N, Peyre P, Song H, Popa I, Ji V, Vignal V (2015) Finite element analysis of laser shock peening of 2050-T8 aluminum alloy. *Int J Fatigue* 70:480–489. <https://doi.org/10.1016/j.ijfatigue.2014.05.015>
43. Le Bras C, Rondepierre A, Ayad M, Rouchausse Y, Gervais M, Valadon S, Berthe L (2021) Novel confinement possibility for laser shock: use of flexible polymer confinement at 1064 Nm wavelength. *Metals* 11:1467. <https://doi.org/10.3390/met11091467>
44. Iordache DM, Oprescu ER, Malea CI, Nițu EL, Crăcănel MO, Bădulescu C (2021) Determination of Johnson-Cook material constants for copper using traction tests and inverse identification, IOP Conf. Ser Mater Sci Eng 1182:012032. <https://doi.org/10.1088/1757-899X/1182/1/012032>
45. Bukelis T, Gaižauskas E, Balachninaïtė O, Paipulas D (2023) Femtosecond IR and UV laser induced periodic structures on steel and copper surfaces. *Surf Interfaces* 38:102869. <https://doi.org/10.1016/j.surfin.2023.102869>
46. Aguilar-Morales AI, Alamri S, Lasagni AF (2018) Micro-fabrication of high aspect ratio periodic structures on stainless steel by picosecond direct laser interference patterning. *J Mater Process Technol* 252:313–321. <https://doi.org/10.1016/j.jmatprotec.2017.09.039>
47. Baumann R, Milles S, Leupolt B, Kleber S, Dahms J, Lasagni AF (2021) Tailored wetting of copper using precise nanosecond direct laser interference patterning. *Opt Laser Eng* 137:106364. <https://doi.org/10.1016/j.optlaseng.2020.106364>
48. Peter A, Lutey AHA, Faas S, Romoli L, Onuseit V, Graf T (2020) Direct laser interference patterning of stainless steel by ultrashort pulses for antibacterial surfaces. *Opt Laser Technol* 123:105954. <https://doi.org/10.1016/j.optlastec.2019.105954>

49. Bonse J, Hohm S, Kirner SV, Rosenfeld A, Kruger J (2017) Laser-induced periodic surface structures—a scientific evergreen. *IEEE J Sel Top Quantum Electron* 23:109–123. <https://doi.org/10.1109/JSTQE.2016.2614183>
50. Zwahr C, Welle A, Weingärtner T, Heinemann C, Kruppke B, Gulow N, Holthaus MG, Lasagni A, Fabián (2019) Ultrashort pulsed laser surface patterning of titanium to improve osseointegration of dental implants. *Adv Eng Mater* 21:1900639. <https://doi.org/10.1002/adem.201900639>
51. Liu B, Zhang J, Zhang C, Xu J (2018) Mechanical integrity of 18650 lithium-ion battery module: packing density and packing mode. *Eng Fail Anal* 91:315–326. <https://doi.org/10.1016/j.engfailanal.2018.04.041>

**Publisher's note** Springer Nature remains neutral with regard to jurisdictional claims in published maps and institutional affiliations.